Chapter 1
Nanophotonics: Dressed Photon Technology for Qualitatively Innovative Optical Devices, Fabrication, and Systems

Motoichi Ohtsu

Abstract This chapter reviews the theoretical picture of the dressed photon by combining the concepts of quantum field theory, optical science, and condensed-matter physics. Based on the exchange of dressed photons, energy transfer to an electric dipole-forbidden energy level is described. Furthermore, the possibility of coupling a dressed photon with a coherent phonon is presented, revealing a novel phonon-assisted process in light–matter interactions in nanometric space. Applications to qualitatively innovative optical devices, fabrication techniques, energy conversion, and systems are exemplified.

1.1 Introduction

Nanophotonics, proposed by the author in 1993 [1–3], is a novel optical technology that utilizes the optical near-field. The optical near-field is the *dressed photons* that mediate the interaction between nanometric particles located in close proximity to each other. Nanophotonics allows the realization of *qualitative innovations* in photonic devices, fabrication techniques, and systems by utilizing novel functions and phenomena enabled by optical near-field interactions that would otherwise be impossible if only conventional propagating light were used. In this sense, the principles and concepts of nanophotonics are completely different from those of conventional wave-optical technology, encompassing photonic crystals, plasmonics, metamaterials, and silicon photonics. This review describes these differences and shows examples of such qualitative innovations.

M. Ohtsu
Graduate School of Engineering, The University of Tokyo, 2-11-16 Yayoi, Bunkyo-ku, Tokyo 113-8656, Japan
and
Nanophotonics Research Center, The University of Tokyo, 2-11-16 Yayoi, Bunkyo-ku, Tokyo 113-8656, Japan
e-mail: ohtsu@ee.t.u-tokyo.ac.jp

M. Ohtsu (ed.), *Progress in Nanophotonics 1*, Nano-Optics and Nanophotonics,
DOI 10.1007/978-3-642-17481-0_1, © Springer-Verlag Berlin Heidelberg 2011

1.2 Background and Principles

The author's primary motivation for proposing nanophotonics was to break the deadlock of optical technology that has existed due to the diffraction limit of the light. In the case of information transmission systems, communications technology roadmaps have claimed that the size of photonic devices should be decreased to several hundreds or tens of nanometers for future high-capacity optical transmission systems [4]; however, this is impossible due to the diffraction limit. In the case of photolithography, although the size of the fabricated patterns should be decreased to several tens of nanometers for mass-production of future semiconductor electronic devices, such as highly integrated DRAMs, this task is difficult due to the diffraction limit. Short-wavelength light sources (excimer lasers, extreme UV light sources, and synchrotron radiation sources) have undergone intense development for use in photolithography systems to decrease the sizes of the fabricated patterns down to the diffraction limit, in other words, to increase the resolution up to the diffraction limit. However, the resulting equipment is extremely large and expensive and consumes a great deal of power, which makes its practical use very difficult.

The focused spots of light are relatively large due to the diffraction limit. Therefore, photonic devices are large and the resolution of photolithography is low. Even if the physical dimensions of these devices could be decreased by nanotechnology, photonic devices cannot be reduced in size beyond the diffraction limit as long as conventional propagating light is used for driving them. To decrease the device size and increase the resolution of photolithography, the size (spatial extent) of the light itself must be decreased.

One promising candidate technology to decrease the size of light is nanophotonics, which was proposed by the author in 1993: If a nanometer-sized particle is illuminated by propagating light, it generates scattered light, which propagates to the far field and exhibits diffraction. However, also generated at the surface of the particle is an *optical near-field*, which is non-propagating light whose energy is localized at the particle surface. Furthermore, the extent of localization is equivalent to the particle size, which is independent of the incident light wavelength, and thus, in the case of a nanometric particle, it is much smaller than the wavelength. Therefore, if the optical near-field is utilized for devices and fabrication, novel technologies that can break through the bounds imposed by the diffraction-limit can be realized, thus enabling *quantitative innovations* in optical technology.

The optical near-field is a *virtual cloud of photons* that always exists around an illuminated nanometric particle. Its energy fluctuation, δE, and duration of the fluctuation, τ, are related by the Heisenberg uncertainty relation, $\tau \delta E \cong \hbar$, where $\hbar$ is Planck's constant divided by 2π. From this relation, the linear dimension of the virtual cloud of photons (the *virtual photons* for short) is given by $r \cong c\tau \cong \hbar c/\delta E$, where c is the speed of light. In the case of visible light illumination (photon energy $\sim$2 eV), r is estimated to be about 100 nm. This means that the effect of the virtual photons at the surface of the illuminated particle is important if the particle is smaller than 100 nm. In other words, the optical properties of sub-micron-sized matter are not free from the effects of virtual photons.

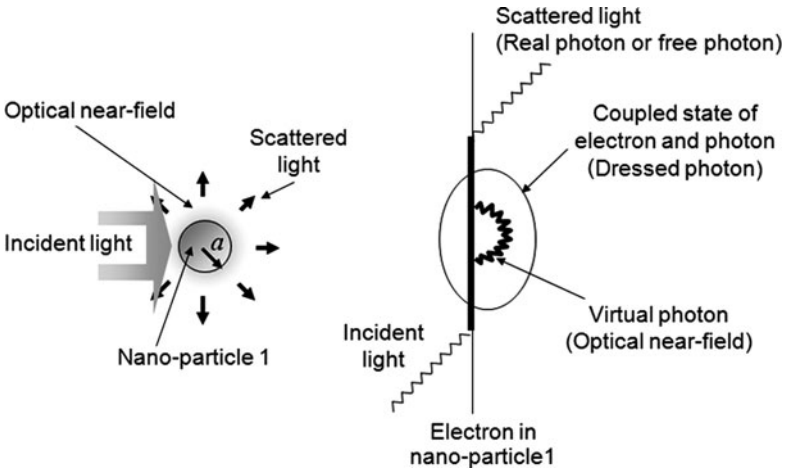

Fig. 1.1 Feynman diagram representing the generation of optical near-fields

This feature of the optical near-field, i.e., the virtual photons, can be most appropriately described by using a Feynman diagram (Fig. 1.1), popularly employed for elementary particle physics. In this figure, a photon is emitted from an electron in the illuminated nanometric particle and can be re-absorbed within a short duration. This photon is nothing more than a virtual photon, and its energy is localized at the surface of the nanometric particle. Independently of this virtual photon, a real photon (also called a free photon) can also be emitted from the electron. This photon is conventional propagating scattered light. Since the virtual photon remains in the proximity of the electron, it can couple with the electron in a unique manner. This coupled state, called a dressed photon, is a quasi-particle from the standpoint of photon energy transfer and has applications to novel nanophotonic devices and fabrication technologies. It is the dressed photon, not the free photon, that carries the material excitation energy. Therefore, the energy of the dressed photon, $h\nu_{\mathrm{dp}}$, is larger than that of the free photon, $h\nu$, due to contribution of the material excitation energy.

To detect the dressed photon, a second nanometric particle should be placed in close proximity to the first particle to disturb the dressed photon on the first particle. This disturbance generates a free photon, which is propagating scattered light that can be detected by a conventional photodetector installed in the far field. This detection scheme suggests that the dressed photon energy is exchanged between the two particles, which can also be represented by a Feynman diagram (Fig. 1.2). That is, after a dressed photon is generated in the first particle, it is transferred to the other particle. It can be transferred back to the first particle again, which means that the dressed photon can be exchanged between the two particles. The detectable free photon is generated in the process of this exchange.

The dressed photon is theoretically described by assuming a multipolar quantum electro-dynamic Hamiltonian in Coulomb gauge and single-particle states in a finite

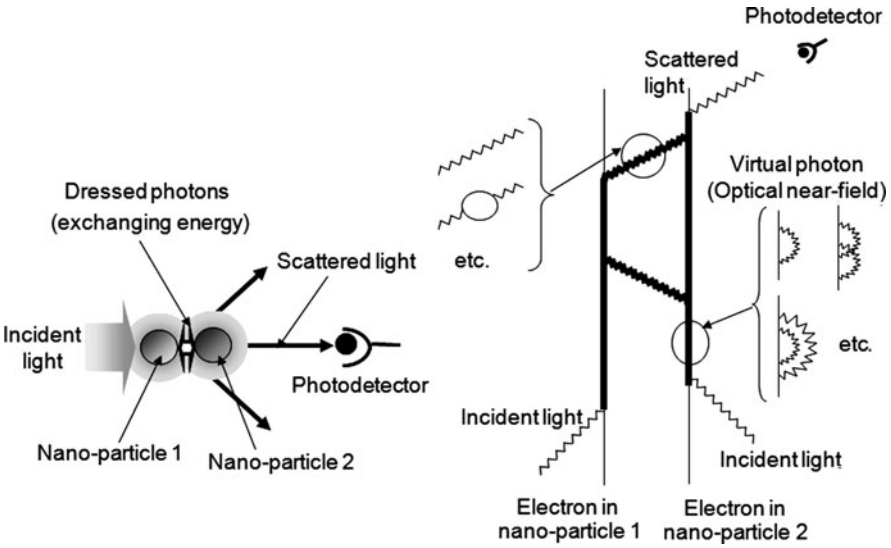

Fig. 1.2 Feynman diagram representing the detection of optical near-fields

nano-system [5]. After a unitary transformation and some simple calculations, its annihilation and creation operators are respectively expressed, in the lowest order, as

$$\tilde{a}_{\vec{k}\lambda} = a_{\vec{k}\lambda} - i N_{\vec{k}} \sum_{\substack{\alpha > F \\ \beta < F}} \left\{ \rho^*{}_{\beta\alpha\lambda} \left(\vec{k} \right) A^\dagger{}_{\alpha\beta} + \rho^*{}_{\alpha\beta\lambda} \left(\vec{k} \right) A_{\alpha\beta} \right\} \tag{1.1}$$

and

$$\tilde{a}^\dagger_{\vec{k}\lambda} = a^\dagger{}_{\vec{k}\lambda} + i N_{\vec{k}} \sum_{\substack{\alpha > F \\ \beta < F}} \left\{ \rho_{\alpha\beta\lambda} \left(\vec{k} \right) A^\dagger{}_{\alpha\beta} + \rho_{\beta\alpha\lambda} \left(\vec{k} \right) A_{\alpha\beta} \right\}, \tag{1.2}$$

where $\vec{k}$ is the wave-number of the free photon, λ is the polarization of a free photon, $N_{\vec{k}}$ is the normalization constant, α and β represent the electronic energy states above and below the Fermi energy level F, $\left(a_{\vec{k}\lambda}, a^\dagger{}_{\vec{k}\lambda}\right)$ and $\left(A_{\alpha\beta}, A^\dagger{}_{\alpha\beta}\right)$ are the annihilation and creation operators of the free photon and an electron–hole pair, respectively, and $\rho_{\alpha\beta\lambda}\left(\vec{k}\right)$ is the Fourier transform of the spatial distribution of the transition dipole, $\rho_{\alpha\beta\lambda}\left(\vec{r}\right)$, of the nanometric particle. Based on this dressed photon picture, interactions between the nanometric particles can be simply described by emission, absorption, and scattering of dressed photons, which provides a physically intuitive picture of the optical near-field interaction between the two particles.

The real system is more complicated because the nanometric subsystem (composed of the two nanometric particles and the dressed photons) is buried in a macroscopic subsystem composed of the macroscopic substrate material and the

macroscopic incident and scattered light fields. A novel theory was developed to avoid describing all of the complicated behaviors of these subsystems rigorously, since we are interested only in the behavior of the nanometric subsystem. In this theory, the macroscopic subsystem is expressed as an exciton–polariton, which is a mixed state of material excitation and electromagnetic fields. Since the nanometric subsystem is excited by an electromagnetic interaction with the macroscopic subsystem, the projection operator method is effective for describing the quantum mechanical states of these systems [6]. As a result of this projection, the nanometric subsystem can be treated as being isolated from the macroscopic subsystem, where the magnitudes of effective interaction energy between the elements of the nanometric subsystem are influenced by the macroscopic subsystem. This local electromagnetic interaction can take place within a sufficiently short duration in which the uncertainty relation allows the exchange of dressed photons non-resonantly, as well as the exchange of a free photon resonantly. The interaction due to the non-resonant process is expressed by a screened potential using a Yukawa function $\exp(-r/a)/r$, which represents the localization of the optical near-field around the nanometric particles. Its decay length a is equivalent to the particle size [6], which means that the extent of localization of the optical near-field is equivalent to the particle size, as was described above. On the other hand, the interaction due to the resonant process is expressed by a conventional spherical wave function, which is mediated by a free photon (a conventional propagating field).

Because the extent of localization of the dressed photon is equivalent to the nanometric particle size, the long-wavelength approximation, which has always been employed for conventional light–matter interaction theory, is not valid. This means that an electric dipole-forbidden state in the nanometric particle can be excited as a result of the dressed photon exchange between closely placed nanometric particles, which enables the operation of novel nanophotonic devices. Details of such devices will be reviewed in Sect. 1.4.

A real nanometric material is composed not only of electrons but also of a crystal lattice. In this case, after a dressed photon is generated on an illuminated nanometric particle, its energy can be exchanged with the crystal lattice, as shown by the Feynman diagram of Fig. 1.3a. By this exchange, the crystal lattice can excite the vibration mode coherently, creating a coherent phonon state. As a result, the dressed photon and the coherent phonon can form a coupled state, as is schematically explained by Fig. 1.3b. The creation operator $\hat{a}_i^\dagger$ of this novel form of elementary excitation is expressed as

$$\hat{a}_i^\dagger = \tilde{a}_i^\dagger \exp\left\{-\sum_{p=1}^{N} \frac{\chi_{ip}}{\Omega_p}\left(b_p{}^\dagger - b_p\right)\right\}, \tag{1.3}$$

where $\tilde{a}_i^\dagger$ is the creation operator of the dressed photon (refer to (1.2)) localized on the ith site of the crystal lattice, N is the number of sites, χ_{ip} is the phonon–photon coupling in mode p at site i, and Ω_p is the eigen-frequency of the phonon mode p. The exponential function in this equation is called a displacement operator,

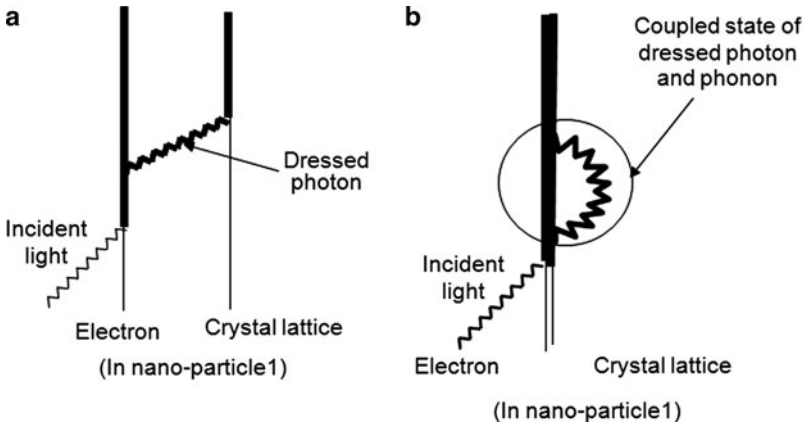

Fig. 1.3 Feynman diagrams representing the coupling of a dressed photon with phonons. (**a**) Generation of a dressed photon and exchange with the crystal lattice. (**b**) A coupled state of a dressed photon and a coherent phonon

composed of the phonon creation and annihilation operators $\left({b_p}^{\dagger} - b_p\right)$. This is an operator representing the creation of the coherent phonon state [7, 8]. This coupled state (*the dressed photon carrying the coherent phonon energy* (DP–CP)) is a quasi-particle and is generated only when the particle size is small enough to excite the crystal lattice vibration coherently. If not, the vibration is incoherent, and thus, its energy is dissipated, heating the particle.

It is easily understood that the energy of the DP–CP, $h\nu_{\mathrm{DP-CP}}$, is higher than that of the dressed photon. It is also higher than the free photon energy, $h\nu_{\mathrm{FP}}$, incident on the nanometric particle. The relation between these energies is represented by

$$h\nu_{\mathrm{FP}} < h\nu_{\mathrm{DP}} < h\nu_{\mathrm{DP-CP}}. \tag{1.4}$$

The first and second inequalities originate from the contribution of the electron and coherent phonon energies, respectively. Novel fabrication techniques allowing qualitative innovations can be developed by utilizing the DP–CP. Several examples of such innovations will be reviewed in Sect. 1.5.

1.3 Fiber Probes, Sensing Systems, and 1 Tb in.$^{-2}$-Density Magnetic Storage Systems

To generate optical near-fields efficiently and reproducibly, selective chemical etching technology has been established for fabricating high-quality fiber probes [9, 10]. This led to the realization of a high-resolution probe with a 1 nm-radius apex, a high-efficiency probe with 10% optical near-field generation efficiency, and other

related devices. Elsewhere in the world, methods involving heating and pulling fiber were most popular at that time [11], although the performance of chemically etched fiber probes was superior. The method used to fabricate these probes was transferred to industry, resulting in high-quality commercial fiber probes. A near-field optical microscope has been developed using these fiber probes, and a variety of ultrahigh-resolution images have been achieved, such as the image of a single-stranded DNA molecule with a resolution greater than 4 nm [12], which is a world record.

A near-field spectrometer has also been developed for diagnosing single semiconductor quantum dots [13], semiconductor devices [14], single organic molecules [15], and biological specimens [16]. Many experimental results on spatially resolved photoluminescence and Raman spectra with 10 nm resolution have been accumulated [17]. Patents have been transferred to industry to produce commercial near-field photoluminescence spectrometers that operate in the ultraviolet-infrared region, at liquid helium-room temperature ranges, and in high magnetic fields [18]. Since their introduction in the market, they have been popularly used in a variety of nanoscience and nanotechnology fields. Instead of using fiber probes, apertureless probes are sometimes used because of their simplicity of fabrication and the possibility of field enhancement. However, it has been demonstrated that apertureless probes cannot realize high resolution due to the scattering of residual propagating light [19].

Technology for fabricating a triple-tapered fiber probe has been developed to increase the optical near-field generation efficiency by up to 1,000 times through efficient excitation of the EH_{11} mode in a fiber [20,21]. This was applied to develop a pyramidal silicon probe on a contact slider for writing and reading in a phase-change optical storage disk system [21,22]. The shortest mark length and the carrier-to-noise ratio were 110 nm and 10 dB, respectively, with a data transmission rate of 2.0 MHz. Using the two-dimensional probe array, the rate was expected to increase to 200 MHz. This and related work triggered the development of an optical near-field assisted magnetic storage system.

The upper limit of the storage density of conventional magnetic storage systems is about 0.3 Tb in.$^{-2}$, which is limited by the thermal instability of the magnetic domains on the disk. To break this limit, an optical near-field was used to locally heat a magnetic domain to decrease the coercivity, followed by immediately applying a magnetic field to the domain to write a pit. With this technique, a storage density as high as 1 Tb in.$^{-2}$ is expected, which meets the requirements of the technology roadmaps of future magnetic storage systems.

To realize such a high-density magnetic storage system, a Japanese national project was organized with academia-industry collaboration, supervised by the author and involving eight Japanese companies [23]. This project developed three main technologies:

(1) *Near-field storage media technology* [24]. Two or three rows of magnetic dots were aligned circumferentially in guide grooves that were drawn using an electron beam mastering method. A process for flattening surfaces was also developed. Nano-patterned media (20 nm in diameter) were fabricated at 30-nm intervals, and individual magnetic dots were grown on them. A self-assembly

method was developed for circumferential alignment using an Si master disk. In addition, regularly aligned dot patterns were obtained with block copolymers. Co/Pd multilayers that had a perpendicular anisotropy of 9.2×10^6 erg/cc were developed, and a magnetization reversal size of 20 nm was obtained by patterning the film into dots.

(2) *Recording technology* [25, 26]. A device made of a baked metallic plate, named a "nano-beak" was developed for generating an optical near-field with a spot diameter of 20 nm with efficiency of several percent. A near-field optical slider head was then fabricated to mount the nano-beak and a solid immersion lens. The slider head ran with a linear velocity higher than 7 nm s^{-1} in a stable manner, maintaining a flying height of 20 nm. An isolated dot of 20 nm in diameter was recorded on a Co/Pd multilayer magnetic nano-patterned medium.

(3) *Nano-mastering technology.* A novel electron beam (EB) technique was developed to converge the EB spot to a diameter of 20 nm with a current density of 8 kA cm^{-2}. Using this technique, master disks were fabricated for 1 Tb $in.^{-2}$-class storage with a groove width of 15 nm and track pitch of 30 nm. The standard deviation of the track pitch was less than 1.5 nm. A formatter was also improved to increase the drawing speed and accuracy.

By assembling these technologies, isolated pits of 20 nm-diameter at 30 nm-pitch were successfully written on a storage disk, corresponding to a storage density of 1.5 Tb $in.^{-2}$ (Fig. 1.4). These technical developments realized a storage density

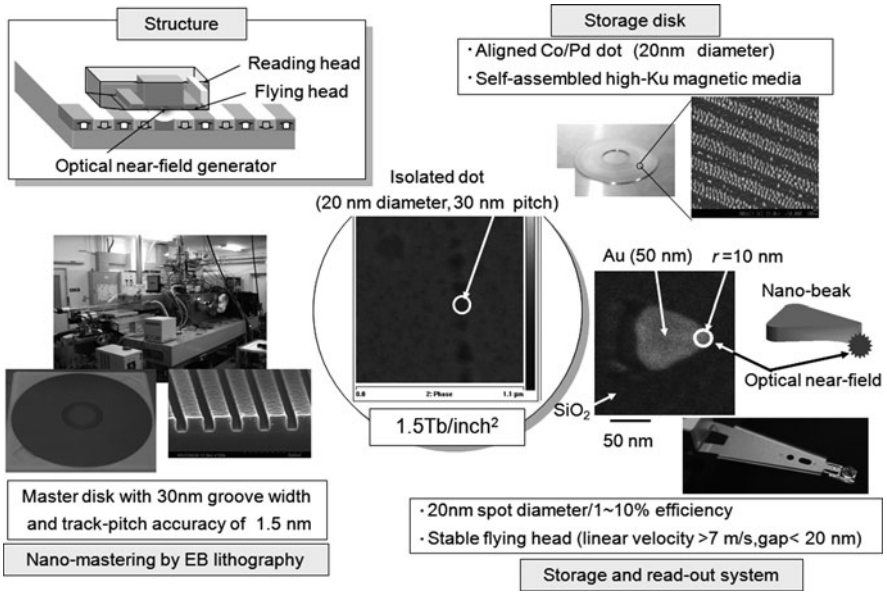

Fig. 1.4 Technologies for optical near-field assisted magnetic storage system with 1.5 Tb $in.^{-2}$ storage density

higher than that dictated by the fundamental limits due to thermal fluctuations. Furthermore, with the recent progress of EB lithography, a track pitch as small as 3.5 nm was achieved in 2010 [27], from which a storage density reaching 10 Tb in.$^{-2}$ can be expected in the near future. A technology roadmap predicting a future storage density as high as 1 Pb in.$^{-2}$ by the year 2025 has also been published [28]. To achieve such quantitative innovations in storage density, this roadmap predicts that conventional memory systems using moving devices (such as flying heads and rotating disks) will be completely replaced by novel solid-state elements using various kinds of nanophotonic devices and their associated integrated circuits. These will be reviewed in the next section.

1.4 Nanophotonic Devices

The size and energy consumption of electronic and optical devices must be reduced to improve the performance of information processing systems and energy conversion systems. It should be noted that conventional electronic devices can hardly meet these requirements because they need electrical wires for connection with external devices to fix the direction of the energy flow and the transmitted signal intensity. This means that they dissipate a large amount of energy in the external macroscopic wires. Furthermore, these electronic wires are susceptible to non-invasive attacks [29]. Conventional optical devices also need connecting lines, such as optical fibers and dielectric optical waveguides, as long as propagating light is used as a signal carrier. Even macroscopic free space in vacuum may play the role of the connecting line here.

Nanophotonics is a promising candidate for meeting the above requirements for two reasons: (1) a signal can be transferred by the dressed photon exchange between nanometric particles without using any wires and (2) a non-invasive attack is impossible because the signal intensity is fixed by the energy dissipation inside the nanometric particles [30]. This section reviews the principles, operations, and applications of these nanophotonic devices.

1.4.1 Basic Devices

Because the long-wavelength approximation is not valid due to the localized nature of the dressed photon (refer to Sect. 1.2), an electron in the nanometric particle can be excited even to an electric dipole-forbidden energy level as a result of the dressed photon exchange between closely spaced nanometric particles, which enables novel nanometer-scale wireless optical devices with dimensions beyond the diffraction-limit, low energy consumption, and resistance to non-invasive attacks.

Figure 1.5 explains the principle of operation. Two semiconductor cubic quantum dots (QD) of different sizes are placed in close proximity to each other. The

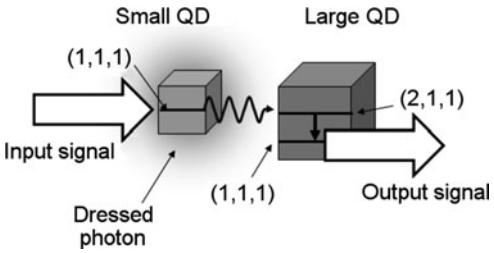

Fig. 1.5 Operating principle of nanophotonic device

small and large QDs are used as input and output ports of the device, respectively. Quantized energy levels of excitons that are relevant to the device operation are also illustrated in this figure. The (1,1,1) exciton energy level in the small QD and the (2,1,1) energy level in the large QD are resonant with each other when the ratio of their sizes is $1 : \sqrt{2}$. However, it should be noted that these levels are electric dipole-allowed and -forbidden, respectively. If the input optical signal is applied to the small QD, an exciton can be excited to the (1,1,1) energy level resulting in the generation of a dressed photon. Then, this dressed photon can excite the exciton to the electric dipole-forbidden (2,1,1) energy level in the large QD because the long-wavelength approximation is not valid. After this excitation, the subsequent fast relaxation from the (2,1,1) to the (1,1,1) energy level in the large QD can block energy back-transfer to the small QD, guaranteeing unidirectional signal transfer from the input to the output port. It should be noted that such energy transfer to the electric dipole-forbidden level has never been realized in conventional optical devices, and thus, Fig. 1.5 represents a qualitative innovation in device operation.

Based on this operating principle, novel nanophotonic devices and their associated integrated circuits have been proposed (Fig. 1.6) [31]. They are connected with conventional macroscopic fiber transmission lines. The integrated circuit includes light emitting devices, functional devices such as optical switches (AND gates), and photodetectors, which are all composed of nanometric particles. By applying the input optical signal through the input terminal, a dressed photon is generated on one particle and is transferred to the adjacent one, and finally, the output signal exits through the output terminal.

An optical switch (an AND gate) (Fig. 1.7) is the first example of the basic devices to be reviewed in this section [32]. Three different-sized QDs are used as input, output, and control ports. By fixing their size ratio to $1 : \sqrt{2} : 2$, they satisfy the resonant condition of Fig. 1.5. When the input signal is applied to the input QD to excite the exciton to the (1,1,1) energy level, the dressed photon exchange allows resonant energy transfer to the electric dipole-forbidden (2,1,1) energy level of the output QD. After subsequent relaxation from the (2,1,1) to (1,1,1) energy level in the output QD, the energy is then resonantly transferred to the (2,1,1) energy level of the control QD. Similar transfer is possible also from the (1,1,1) energy level of the input QD to the (2,2,2) energy level of the control QD. Finally, all the energies are transferred to the control QD, and the exciton relaxes to the (1,1,1) energy level to be dissipated to the external heat bath. This means that the output QD does

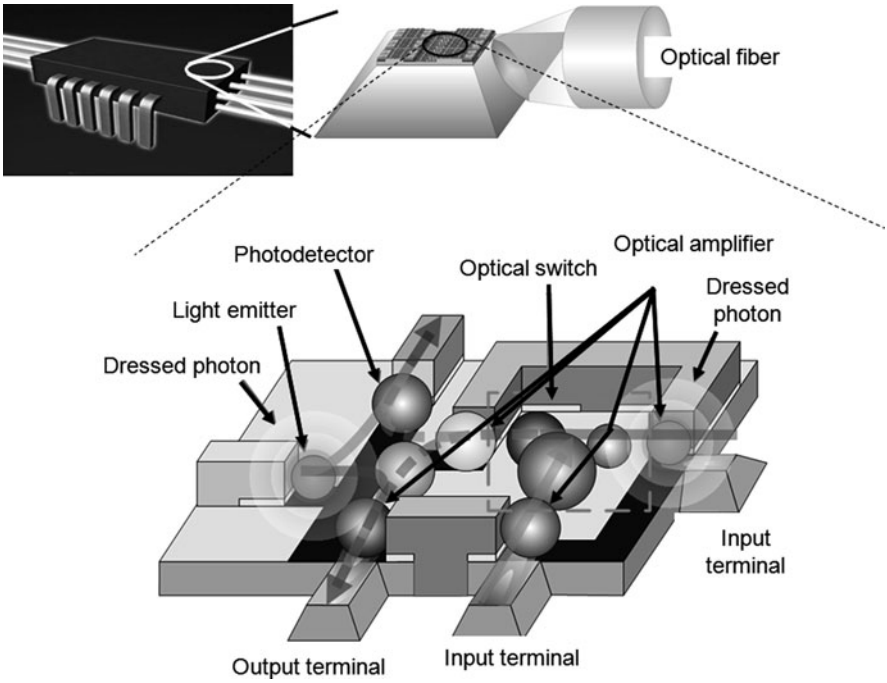

Fig. 1.6 Integrated circuit of nanophotonic devices

not generate any output signals, which corresponds to the off-state of the switch (Fig. 1.7a). To turn the switch on, the control signal is applied to the control QD to excite an exciton to its (1,1,1) energy level (Fig. 1.7b). This excitation prohibits any energy transfers from the other QDs to the control QD due to the shifts of the energy levels of the control QD originating from the many-body effect of the exciton. As a result, an output signal is generated from the (1,1,1) energy level of the output QD.

A switching operation has been experimentally confirmed by using cubic CuCl QDs with sizes 4, 6, and 8 nm separated from each other by 3 nm. They were grown in a self-assembled manner in an NaCl crystal. Figure 1.8 shows the experimental result obtained at a temperature of 5 K. By applying the control signal pulse, the input signal was transferred to the output QD to generate the output signal, which was detected by a near-field spectrometer (Fig. 1.8a). The magnified output pulse shape in Fig. 1.8b represents a 25 ps rise time, determined by the time constant T of the dressed photon exchange, which is inversely proportional to the optical near-field interaction energy represented by the Yukawa function. The fall time is 4 ns, which is determined by the carrier lifetime τ_c, i.e., the time constant of the energy dissipation from the (1,1,1) energy level of the control QD to the heat bath. The fall time can be decreased by extracting the energy of the (1,1,1) energy level of the control QD into the other energy levels in additional QDs to be placed adjacent to it. The solid curve of the magnified output pulse profile in Fig. 1.8b represents the

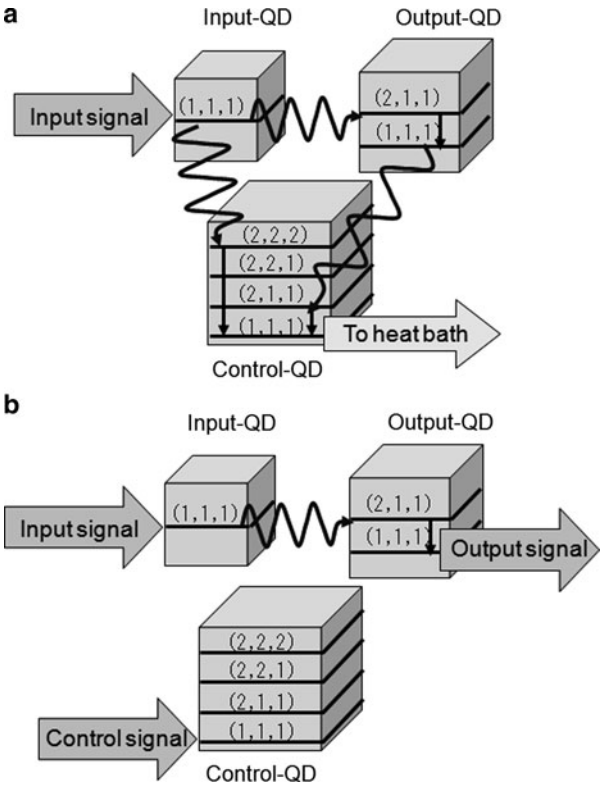

Fig. 1.7 An optical switch. (**a**) Off state. (**b**) On state

value calculated by the dressed photon theory, which agrees well with the experimental values. The oscillatory behavior in the solid curve is due to the residual bi-directional energy transfer by the dressed photon exchange between the input and output QDs.

To demonstrate room-temperature operation necessary for practical industrial applications, three layers of InAs QDs were grown in a size- and position-controlled manner by a molecular beam epitaxy method. After the growth, the sides of the layered structure were removed by phonon-assisted photolithography to form a switching device module (Fig. 1.9a-refer to Sect. 1.5.2 and also to Fig. 1.11a). Device operation at a wavelength of 880 nm has been confirmed at a temperature as high as 210 K (Fig. 1.9b). Recently fabricated InAs QDs exhibit a very strong photoluminescence signal at 273 K, showing the potential for room-temperature operation for practical switching devices. By slight modification of the device structure, switching operation was confirmed also by using two closely spaced ZnO quantum wells in a ZnO nanorod [33].

The second example is a NOT gate, illustrated in Fig. 1.10 [34]. Small and large QDs are used as output and input ports, respectively. Since their size ratio slightly

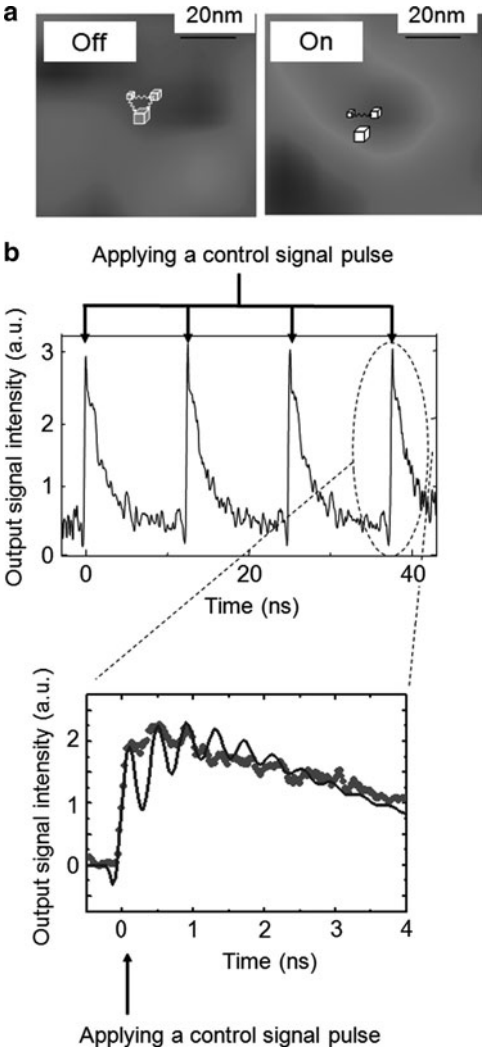

Fig. 1.8 Experimental results of switching operation using cubic CuCl QDs at a temperature of 5 K. (**a**) Near-field optical images of the output signal intensity. (**b**) Temporal behavior of the output signal intensity and its magnified profile. The *solid curve* and *closed circles* represent theoretical and experimental values, respectively

deviates from $1 : \sqrt{2}$, the energy levels of the two QDs are off-resonant. CW optical energy, serving as a power supply for the device, is applied to the (1,1,1) energy level of the output QD to generate the dressed photon. However, due to the off-resonant condition, the generated dressed photon is not transferred to the (2,1,1) energy level of the input QD. As a result, the dressed photon is directly extracted as an output signal from the output QD (Fig. 1.10a). This represents output signal generation in the absence of the input signal.

By applying an input signal to excite an exciton to the (1,1,1) energy level of the input-QD, the linewidth of the (2,1,1) energy level of the input QD is broadened due to the decrease in the phase-relaxation time of the exciton induced by carrier–carrier

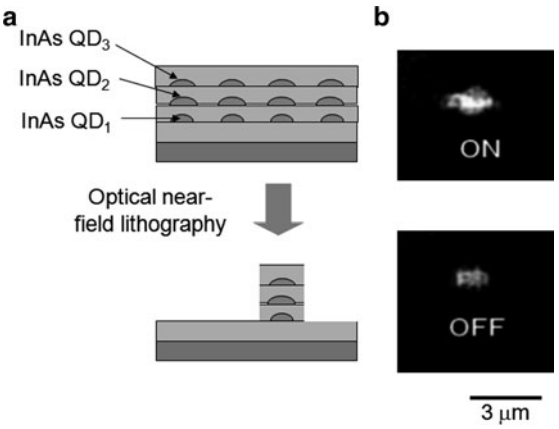

Fig. 1.9 An optical switch using InAs QDs for room-temperature operation. (**a**) Schematic cross-sectional profile of the three-layered QDs. (**b**) Near-field optical image of the output signal intensities for on and off states

scattering. This broadening allows this energy level to be made resonant with the (1,1,1) energy level of the output QD, by which the dressed photon, generated by the CW light, is transferred from the (1,1,1) energy level of the output QD to the (2,1,1) energy level of the input QD. After this transfer and subsequent relaxation to the (1,1,1) energy level in the input QD, the energy is dissipated to the heat bath, resulting in no dressed photon generation from the output QD. This means that no output signal is extracted even though the input signal is applied to the input QD (Fig. 1.10b). Such mutually anti-correlated relation features between the input and output signals, as shown by Fig. 1.10a, b, represent a NOT gate operation.

The NOT gate operation was experimentally confirmed by using CuCl QDs, as in the case of the nanophotonic switch. Figure 1.10c shows the temporal behavior of the output signal intensity, which decreases when applying the input signal pulse. For room-temperature operation, two layers of InAs QDs were grown in a size- and position-controlled manner, as in the case of the nanophotonic switch. After the growth, the sides of the layers were removed by phonon-assisted photolithography (refer to Sect. 1.5.2) to form a two-dimensional array of NOT gate modules [34]. Figure 1.11a shows an AFM image representing a two-dimensional array of more than 100 NOT gate devices which were fabricated within a substrate area of $5\,\mu m \times 5\,\mu m$. Figure 1.11b shows the temporal behavior of the signal intensity generated at a temperature of 298 K.

By combining AND and NOT gate operations, NOR, OR, and NAND gates can be assembled (Fig. 1.12), allowing a complete set of logic gates to be realized for application to future information processing systems. Fan-out F is an important parameter that represents the ability to series-connect multiple nanophotonic devices. It is given by $F = \tau_c/2T$, where τ_c and T are the carrier lifetime and the time constant of dressed photon exchange, respectively. In the case of the above-mentioned nanophotonic switch and NOT gate composed of CuCl QDs, the value of F is 10 because τ_c and T are 2 ns and 100 ps, respectively. In the case of InAs QDs, it is 5 because τ_c and T are 1 ns and 100 ps, respectively. These values of F are sufficiently large for practical applications.

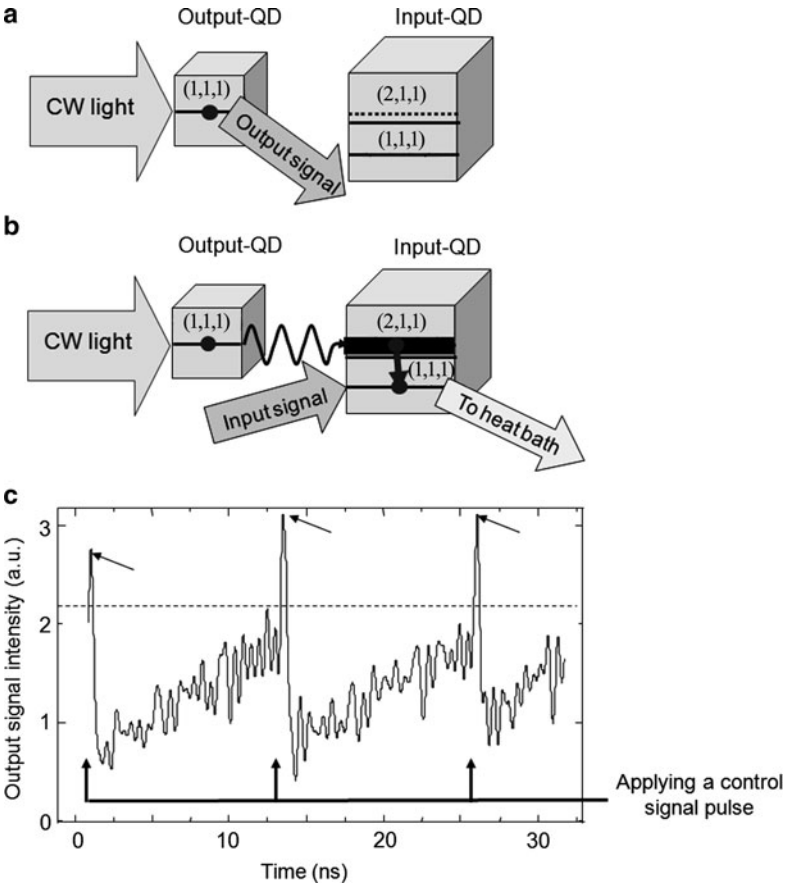

Fig. 1.10 A NOT gate. (**a**), (**b**) Principles of operation. (**c**) Experimental results obtained using cubic CuCl QDs. Three peaks indicated by *arrows* represent artifact signals induced by the pulsed laser used as an input signal source

As was illustrated in Fig. 1.5, the photon energy $h\nu_2$ of the output signal is lower than that of the input signal $h\nu_1$. For up-conversion of the output signal frequency ν_2 to ν_1, the nanophotonic switch of Fig. 1.7 can be used, as illustrated in Fig. 1.13. For designing a frequency up-converter, it should be noted that the size of the QDs can be easily adjusted, so that the output signal frequency is tuned to the input signal frequency ν_1 of the nanophotonic device 1 in this figure. With this adjustment, the output signal of the nanophotonic device 2 is applied to the control QD of the up-converter, whereas a CW optical signal is applied to the input QD. Via the dressed photon exchange between the three QDs in the up-converter and subsequent fast relaxation, it is easy to grasp from Fig. 1.13 that an output signal with frequency ν_1 is generated from the output QD.

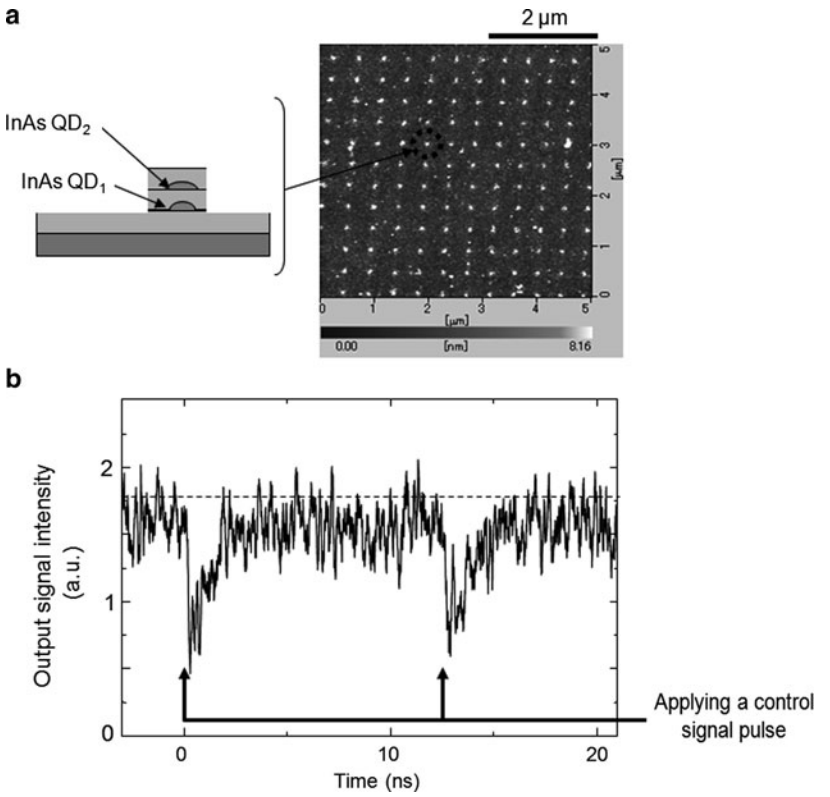

Fig. 1.11 A NOT gate using InAs QDs for room-temperature operation. (**a**) AFM image of a two-dimensional array of the NOT gates. (**b**) Temporal behavior of the output signal intensity

In addition to the basic logic gate devices reviewed above, a variety of novel devices are made possible by nanophotonics. A light emitting device, namely, an optical pulse generator, has been invented by using a chain of closely spaced QDs. Cooperative behavior of the induced electric dipoles in these QDs has been used to realize Dicke's super-radiant photon emission [35]. An optical buffering device has also been invented by utilizing bi-directional energy transfer due to the dressed photon exchange. Its operation has been experimentally confirmed by using a multi-quantum well in the ZnO nanorod [33]. Furthermore, optical buffering operation has also been confirmed by utilizing a time-delayed energy concentration feature of a so-called optical nano-fountain (refer to Fig. 1.15b) [36]. For connecting nanophotonic devices in the integrated circuit of Fig. 1.6, a nano-dot coupler has been invented based on the dressed photon exchange, and its successful operation has been confirmed by using a chain of CdSe QDs [37]. A novel method of fabricating a chain of ZnO QDs has been developed by utilizing DNA as a template [38].

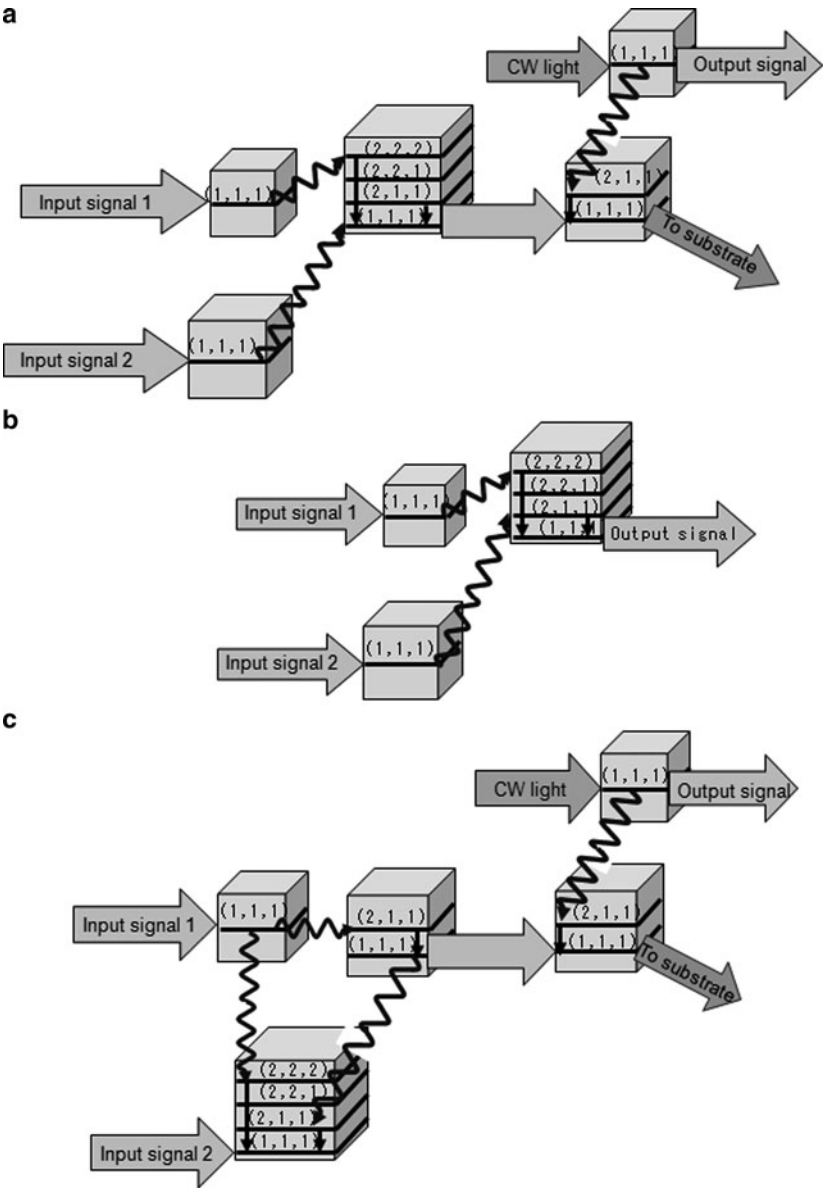

Fig. 1.12 (**a**) NOR, (**b**) OR, and (**c**) NAND gates

1.4.2 Input and Output Terminals

Input and output terminals are used to connect the nanophotonic device in the integrated circuit with external macroscopic photonic devices. The input terminal is used to convert the incident propagating light (free photons) to the optical near-field

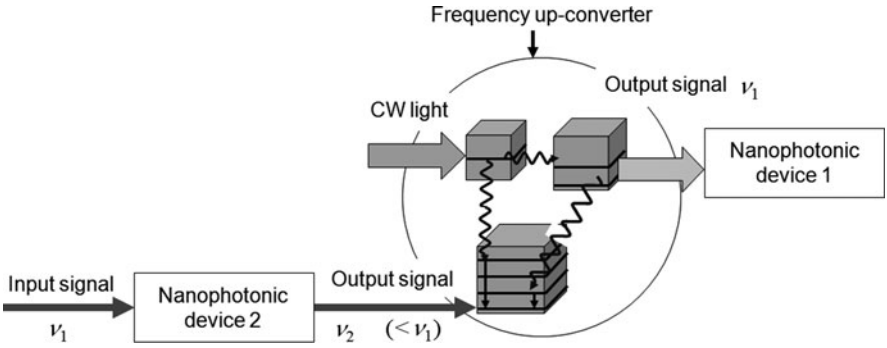

Fig. 1.13 A frequency up-converter

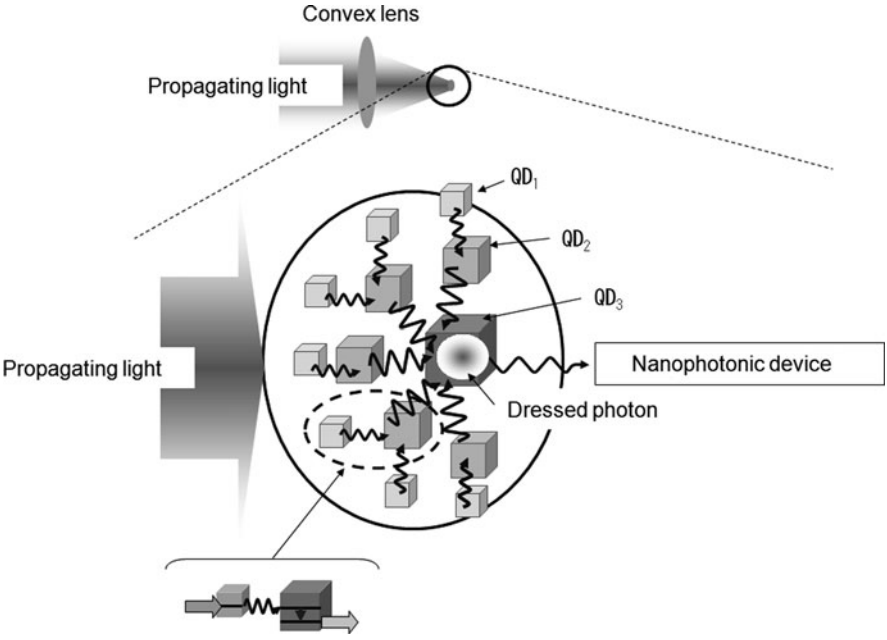

Fig. 1.14 An optical nano-fountain

(dressed photons). A novel device called an *optical nano-fountain* has been invented for such conversion; its operation is similar to that of the light-trapping antennae in light-harvesting bacteria [39]. As illustrated in Fig. 1.14, it utilizes the dressed photon exchange between QDs of different sizes and subsequent fast relaxation. Finally, all of the energy of the incident propagating light is concentrated to the largest QD located at the center, resulting in the generation of dressed photons. The conversion efficiency from the free to the dressed photon energies is high because the energy is dissipated only through relaxation from upper to lower quantized energy levels in each QD.

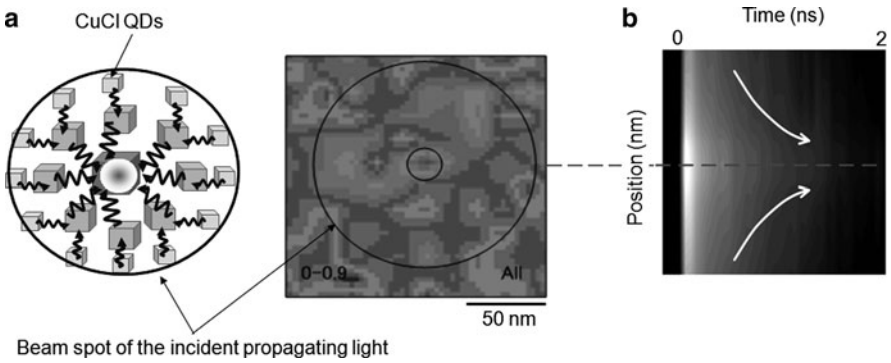

Fig. 1.15 Experimental results of the optical nano-fountain realized using CuCl QDs. (**a**) Near field-optical image of the output optical spot. (**b**) Temporal behavior of the optical energy concentration

Proper device operation has been experimentally confirmed by using CuCl QDs at low temperature, as with the nanophotonic switch and the NOT gate. Figure 1.15a shows an output optical spot with a diameter of less than 10 nm measured by a near-field spectrometer; in contrast, the spot size of the incident light (wavelength: 325 nm) was as large as 150 nm. This means that the equivalent numerical aperture of focusing is much larger than unity. Figure 1.15b shows the temporal behavior of the optical energy transfer to the central largest QD, whose time constant is governed by the time constant T for dressed photon exchange.

For room-temperature operation, multi-layered InAs QDs were grown by molecular beam epitaxy in a size- and position-controlled manner (Fig. 1.16) [40], as with the basic devices reviewed in Sect. 1.4.1. A layer of large QDs was sandwiched by 30 layers of small QDs. The dressed photons generated by applying the input propagating light to the small QDs were transferred to the large QDs. The resultant photoluminescence intensity emitted from the large QDs (wavelength: 1,581 nm) was confirmed to be 40 times larger than that from a solitary layer of large QDs.

An output terminal can be easily realized by fixing a metallic nanometric particle in close proximity to the output QD of a nanophotonic device. The dressed photon is transferred from the output QD to the metallic nanometric particle to generate a scattered free photon, as a result of the large electric dipole and the fast relaxations of phase and energy in the metallic nanometric particle. This device operation was confirmed by fixing a gold nanometric particle on the top of a cap layer of InAs QDs. Figure 1.17 shows the two-dimensional array of scattered light spots originating from the gold particles on the two-dimensionally arrayed InAs QDs. An increase in the photoluminescence intensity from the InAs QDs is due to the gold nanometric particles. This is because the impedance due to the fast relaxations of phase and energy are matched to that of free space, resulting in efficient energy conversion from the dressed photon to the free photon.

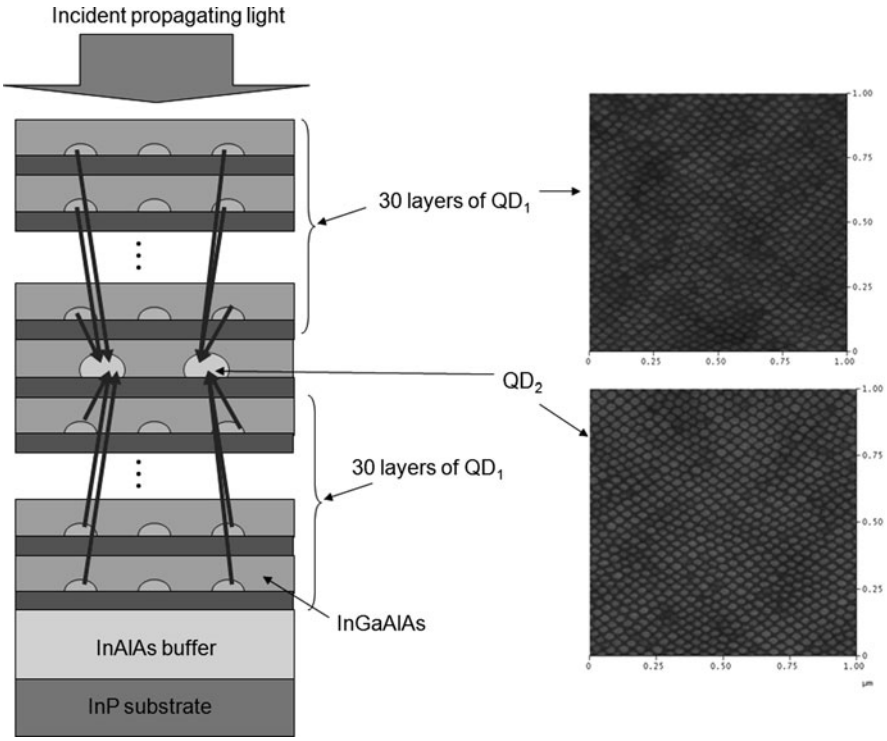

Fig. 1.16 Cross-sectional profile and AFM images of the optical nano-fountain using InAs QDs for room-temperature operation

1.4.3 Unique Features and Application to Information Processing Systems

Nanophotonic devices have several unique features, by which their predominance over conventional photonic devices has been established for application to next-generation information processing systems. One feature is undoubtedly their nanometer-scale dimensions beyond the diffraction limit, which is an example of a quantitative innovation of optical technology. However, it should be noted again that the true nature of nanophotonic devices involves their ability to realize qualitative innovations, originating from their unique features. These features are:

(1) *Low heat generation and low energy dissipation*. A nanophotonic device dissipates energy only through the relaxation from an upper electric dipole-forbidden energy level to a lower electric dipole-allowed energy level. The rate of relaxation is expressed as

$$\Gamma = 2\pi |g(\omega)|^2 D(\omega), \tag{1.5}$$

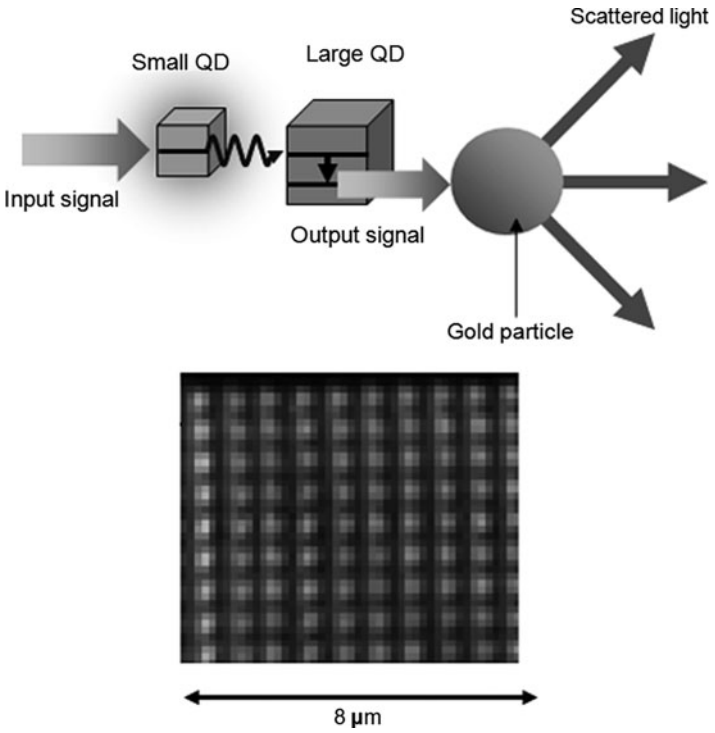

Fig. 1.17 Two-dimensional array of scattered light spots originating from the gold particles on two-dimensionally arranged InAs QDs

where $g(\omega)$ and $D(\omega)$ represent the exciton–phonon coupling energy divided by $\hbar$ and the phonon density of states, respectively. The value of Γ depends on the size and structure of the QD. Typical values are, for example, 10 meV and 50 meV for CuCl and InAs QDs, respectively, from which the magnitude of the heat generated from a nanophotonic switch is estimated to be about 10 pW for an operating frequency of 1 GHz. On the other hand, it is estimated to be as high as 100 nW in the case of a conventional electronic transistor device with an operating frequency of 1 GHz. This comparison shows that the heat generation is only 10^{-5} times that of conventional electronic devices, which is advantageous in building a highly integrated circuit of nanophotonic devices.

For more detailed estimation of the energy dissipation, the relation with the error ratio (the bit error rate) should be discussed. By referring to Fig. 1.5, the output signal is correctly generated only when the input signal is transferred from the (1,1,1) energy level of the small QD to the (2,1,1) energy level of the large QD, with subsequent relaxation to the (1,1,1) energy level of the large QD. An invalid output is generated if the input signal is transferred directly to the (1,1,1) energy level in the large QD without going through the (2,1,1) energy level. The possibility of this direct transfer depends on the value of the relaxation rate Γ. Based

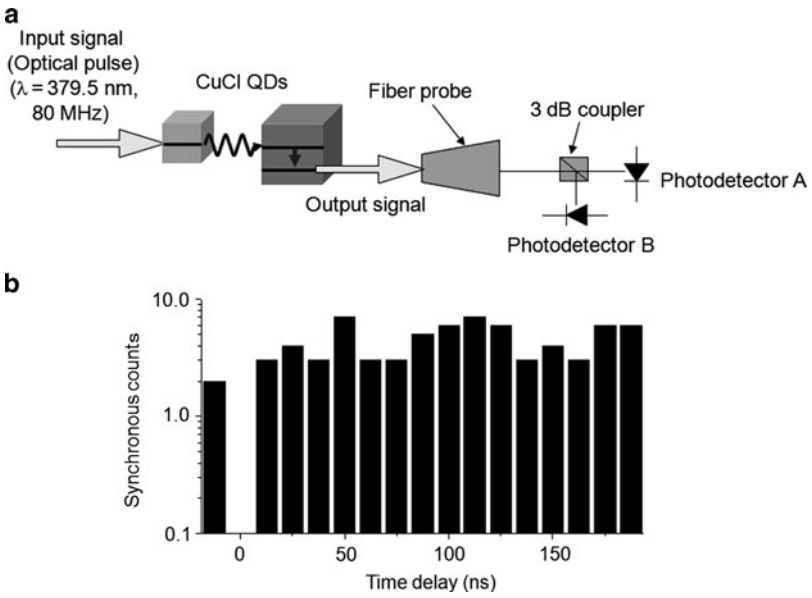

Fig. 1.18 Single-photon operation of a nanophotonic device using CuCl QDs. (**a**) Experimental setup. (**b**) Measured relation between the time delay and the number of synchronous counts

on a master-equation analysis, it was found that the error ratio due to this invalid output remained lower than 10^{-6} if the magnitude of the energy dissipation due to Γ in the large QD was larger than 25 μeV [41]. This small value of energy dissipation suggests that the heat generation of nanophotonic devices could be substantially lower than that of conventional electronic logic devices [42]. In fact, this low energy dissipation could be as low as that of the computational operations in biological systems [43].

(2) *Single photon operation*. The single photon operation capability of nanophotonic devices has been confirmed by the Hanbury Brown and Twiss method (Fig. 1.18a) [44], where two closely spaced CuCl QDs were used at 15 K [45]. The thick black bars in Fig. 1.18b show the measured results of the synchronous counts with different electric time-delays, which were acquired by using two synchronous photodetectors. In this figure, the value of the synchronous count is very small at the time origin ($t = 0$). This clear anti-bunching feature indicates that the two QDs were acting as a single photon emitter. A 99.3% plausibility of single-photon emission was confirmed with 99.98% accuracy. Such clear single-photon operation was attributed to three blockade mechanisms: (1) If one tries to generate two excitons in the small QD, its (1,1,1) energy level is shifted by -30 meV, which corresponds to the binding energy of the exciton molecule. This implies that the energy level becomes detuned from the input signal, and thus, exciton generation is prohibited. (2) Only a single exciton is transferred from the smaller QD to the larger QD by dressed photon exchange because the

(1,1,1) energy level of the small QD becomes off-resonant with respect to the (2,1,1) energy level of the large QD if multiple excitons are generated in the small QD. (3) After the energy transfer, a single exciton can remain stable in the large QD due to the large binding energy of the exciton molecule. Hence, a single photon is emitted from the (1,1,1) energy level of the large QD after fast relaxation from the (2,1,1) energy level.

(3) *Resistance to non-invasive attacks*. As was pointed out at the beginning of this section, conventional electronic and optical devices need electrical or optical wires to dissipate their energies toward the external macroscopic wires to fix the output signal intensity. Since it is straightforward to monitor the signals transmitted through these wires by using conventional electrical or optical sensing probes, non-invasive attacks are possible [29]. In contrast, a nanophotonic device dissipates the energy only through the relaxation from the higher to the lower energy levels in the QD. Because the energy is dissipated by non-radiative relaxation to the crystal lattice vibration (phonon) in the QD (refer to (1.5)) and also because its magnitude is very low, non-invasive attacks are extremely difficult, and thus, the tamper resistance is high [30, 46]. This is advantageous for maintaining security in information processing systems.

In addition to the unique features outlined above, further advantages of nanophotonic devices over conventional optical devices include the possibility of novel logic operations and correlation functions. Additionally, for application to information transmission systems, their operating wavelengths are compatible with WDM systems. Although the operating speed of current WDM systems is about 10 Gbps, higher speeds are expected in the near future by decreasing the fall time (refer to Fig. 1.8b).

Based on these advantages, nanophotonic devices have already been employed for demonstrating prototype novel information processing systems. An example is a highly integrated content addressable memory (CAM) of an optical router system, whose main component is a routing table [47]. The global sum system (the input port of the routing table) was assembled by using an optical nano-fountain (refer to Sect. 1.4.2). As shown in Fig. 1.19a, three small CuCl QDs of different sizes were used as input ports, and a large QD was used as an output port. This figure shows the photoluminescence spectral profiles of the three inputs and the output signals, showing that the output spectral intensity is proportional to the number of bits of the input signals. It demonstrates that this device worked as a three-bit digital-to-analog converter, and thus, the global sum operation was confirmed. For the broadcast system (the output port of the routing table), three nanophotonic switches were used, as shown in Fig. 1.19b. The input signals applied to the input ports of three switches were transferred to their output ports at the moment the control signal pulse was applied. This represents the operation of a three-channel broadcast system. These experimental results demonstrated successful operation of a highly integrated CAM that is much more effective than the huge, high-power-consumption conventional optical router systems.

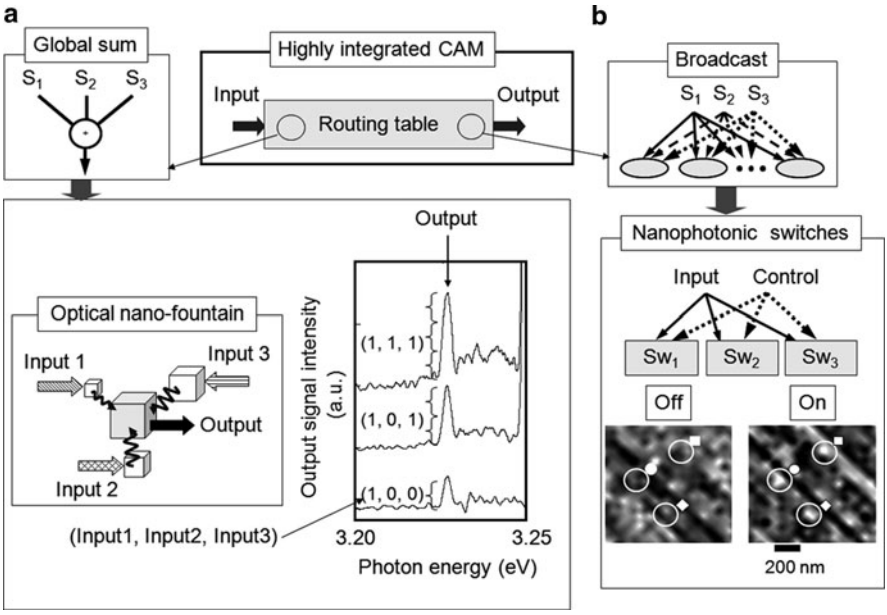

Fig. 1.19 Demonstration of content addressable memory (CAM). (**a**) Global sum system realized by using an optical nano-fountain with three input-ports. (**b**) Broadcast system realized by using three nanophotonic switches

1.5 Nanophotonic Fabrication

The unique phenomena originating from dressed photon exchange have been applied also to the development of novel high-resolution fabrication techniques. As has been described in Sect. 1.2 (refer to (1.3) and (1.4) and Fig. 1.3), the principle of fabrication utilizes the dressed photon, which carries the coherent phonon energy (DP–CP). Several examples are reviewed in this section.

1.5.1 Photochemical Vapor Deposition

Photochemical vapor deposition (PCVD) involves depositing particles or films on a substrate by photo-dissociating organic molecules. Before reviewing a novel PCVD method using the DP–CP, the principle of conventional PCVD is described first, taking metallic Zn deposition as an example. For this deposition, a popularly employed metal-organic molecule is gaseous diethylzinc (DEZ), whose photo-absorption energy E_{abs} and dissociation energy E_{dis} are 4.59 eV and 2.26 eV, respectively. The molecule stably remains in the lowest energy state $\left|E_g; el\right\rangle \otimes |E_l; vib\rangle$, where $\left|E_g; el\right\rangle$ and $|E_l; vib\rangle$ represent the ground electronic state and the lowest

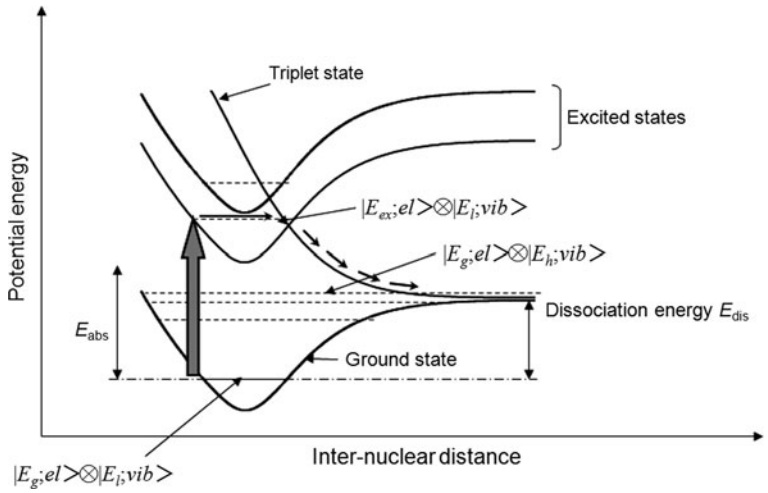

Fig. 1.20 Energy levels of electrons and molecular vibrations

molecular vibrational energy state, respectively (Fig. 1.20). To dissociate the molecule, the simplest way is to excite it to the state $|E_g;el\rangle \otimes |E_h;vib\rangle$ (where $|E_h;vib\rangle$ is a higher molecular vibrational energy state), whose energy is higher than E_{dis}. However, optical excitation is not possible because the transition from $|E_g;el\rangle \otimes |E_l;vib\rangle$ to $|E_g;el\rangle \otimes |E_h;vib\rangle$ is electric dipole-forbidden. Thermal excitation is also very difficult because the molecule must be heated up to an extremely high temperature. To make the dissociation possible, the conventional method is to optically excite the molecule to the excited electronic state $|E_{\text{ex}};el\rangle \otimes |E_l;vib\rangle$, whose energy is much higher than E_{dis}. This is possible because the transition from $|E_g;el\rangle \otimes |E_l;vib\rangle$ to $|E_{\text{ex}};el\rangle \otimes |E_l;vib\rangle$ is electric dipole-allowed. This excitation process is called *adiabatic* because vibrational motions of heavy nuclei are not excited, and these nuclei stay in the lowest vibrational state. Because of this, the Born–Oppenheimer approximation is effective.

This adiabatic PCVD requires short-wavelength light with a photon energy higher than E_{abs} (270 nm wavelength in the case of DEZ), which corresponds to the energy difference between the $|E_{\text{ex}};el\rangle \otimes |E_l;vib\rangle$ and $|E_g;el\rangle \otimes |E_l;vib\rangle$ states. After the molecule is excited to the $|E_{\text{ex}};el\rangle \otimes |E_l;vib\rangle$ state by absorbing this photon, it transits to the triplet state. By this transition, the inter-nuclear distance increases to infinity, resulting in dissociation of the molecule and deposition of dissociated Zn atoms on the substrate.

Instead of the conventional adiabatic PCVD described above, the DP–CP generated at a fiber probe tip enables a novel PCVD because the molecule can transit from $|E_g;el\rangle \otimes |E_l;vib\rangle$ to $|E_g;el\rangle \otimes |E_h;vib\rangle$ by absorbing the DP–CP energy even though the transition is electric dipole-forbidden. If the DP–CP energy $h\nu_{\text{DP–CP}}$ is higher than E_{dis}, transfer of a single DP–CP from the fiber probe tip to the molecule

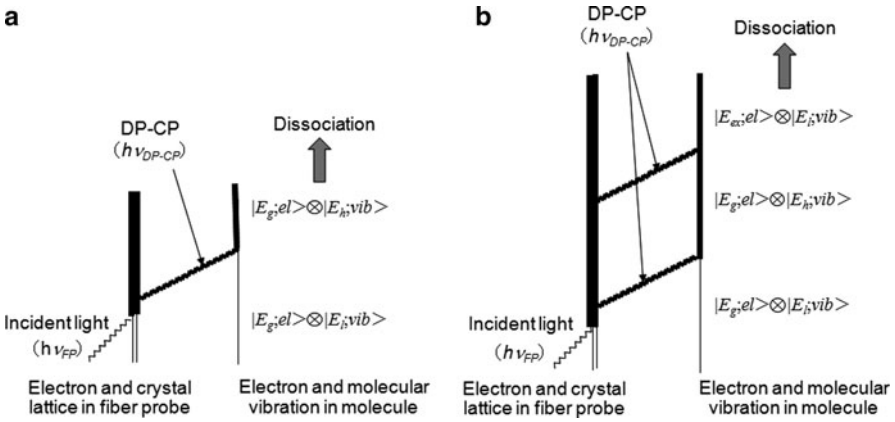

Fig. 1.21 Feynman diagram of DP–CP energy transfer from a fiber probe tip to a molecule. (**a**) and (**b**) show single-step and two-step dissociations, respectively

is sufficient for dissociation, as is schematically explained by the Feynman diagram of Fig. 1.21a. When, $h\nu_{\mathrm{DP-CP}} < E_{\mathrm{dis}}$ multiple DP–CP transfer is required for dissociation, by which the molecule can be excited to the excited electronic state $|E_{\mathrm{ex}}, el\rangle \otimes |E_l, vib\rangle$. Figure 1.21b shows the case where two DP–CPs are transferred, i.e., two-step excitation of the molecule for dissociation. These excitation processes are not adiabatic because vibration modes of the nuclei are excited by the coherent phonon which couples with the dressed photon. Thus, these processes are named *nonadiabatic* or *phonon-assisted*. For these processes, an explanation based on Fig. 1.20 is not valid because the inter-nuclear distance is no longer an independent variable. One technical advantage of these processes is that a high-power-consumption short-wavelength light source is not required. In principle, one can use a longer-wavelength light source even if its photon energy is lower than E_{dis}, which represents a qualitative innovation of this novel PCVD.

Figure 1.22a–c show AFM images of the nanometric Zn particles deposited on a sapphire substrate as a result of dissociating DEZ molecules by the phonon-assisted PCVD using ultraviolet ($h\nu_{\mathrm{FP}} = 3.81\,\mathrm{eV}$; wavelength = 325 nm), blue ($h\nu_{\mathrm{FP}} = 2.54\,\mathrm{eV}$; wavelength = 488 nm), and red ($h\nu_{\mathrm{FP}} = 1.81\,\mathrm{eV}$; wavelength = 684 nm) light sources, respectively, for generating the DP–CP at the fiber probe tip [48]. On the other hand, Fig. 1.22d is an image of a nanometric Zn particle deposited by dissociating Zn(acac)2 molecules [49]. It should be noted that this molecule is optically inactive, i.e., adiabatic dissociation is not possible; however, it was successfully dissociated by the phonon-assisted process.

Figure 1.23 shows the relation between the photon flux I of the light incident on the fiber probe tip for generating the DP–CP and the deposition rate R of the Zn nanometric particles on the substrate. It can be expressed as

$$R = aI + bI^2 + cI^3 + \cdots, \tag{1.6}$$

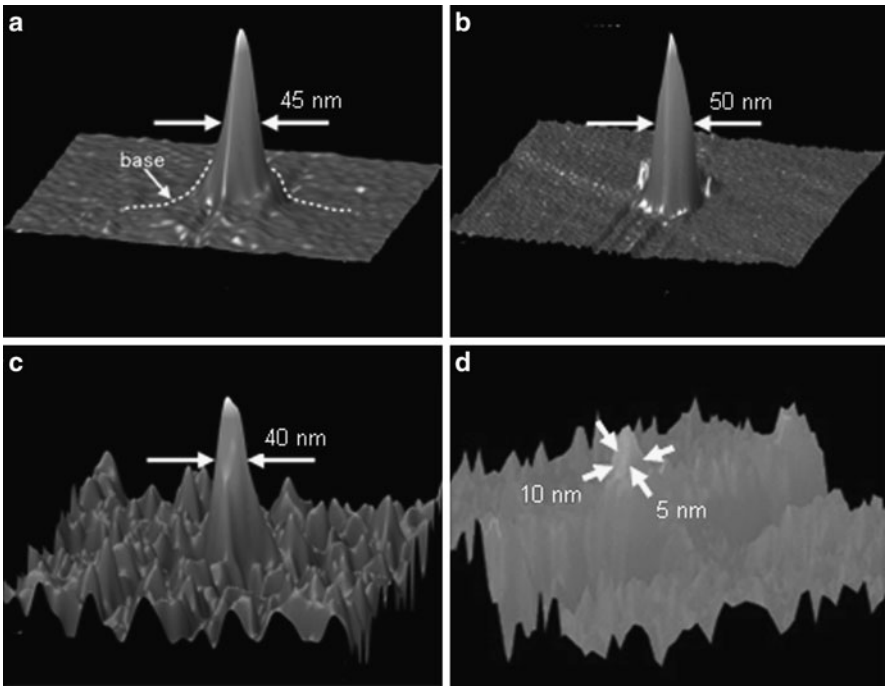

Fig. 1.22 AFM images of nanometric Zn particles deposited on a sapphire substrate by phonon-assisted PCVD using (**a**) ultraviolet, (**b**) blue, and (**c**) red light sources. (**d**) is an image of a nanometric Zn particle deposited by dissociating optically inactive Zn(acac)2 molecules

where the first, second, and third terms represent single-, two-, and three-step excitation by the DP–CP, respectively. Closed triangles in this figure represent the experimental results obtained by using the ultraviolet light source of Fig. 1.22a. Since its photon energy $h\nu_{\mathrm{FP}}$ is higher than E_{dis}, single-step excitation is sufficient to dissociate the DEZ molecules. The experimental results are fitted by the solid line $R = aI$. Since the photon energy $h\nu_{\mathrm{FP}}$ of the blue light (Fig. 1.22b) is still higher than E_{dis}, single-step excitation is sufficient here, too. However, by increasing the incident light intensity I, two-step excitation becomes possible. The experimental results (closed squares) are fitted by the solid curve $R = aI + bI^2$. In the case of the red light (Fig. 1.22c), the photon energy $h\nu_{\mathrm{FP}}$ is lower than E_{dis}; thus, two-step excitation is essential for dissociation. By increasing I, even three-step excitation becomes possible. The experimental results (closed circles) are fitted by the solid curve $R = bI^2 + cI^3$. Theoretical studies have proved that the ratios between the coefficients of (1.6) satisfy the relation

$$\frac{b}{a} = \frac{c}{b} = \cdots. \tag{1.7}$$

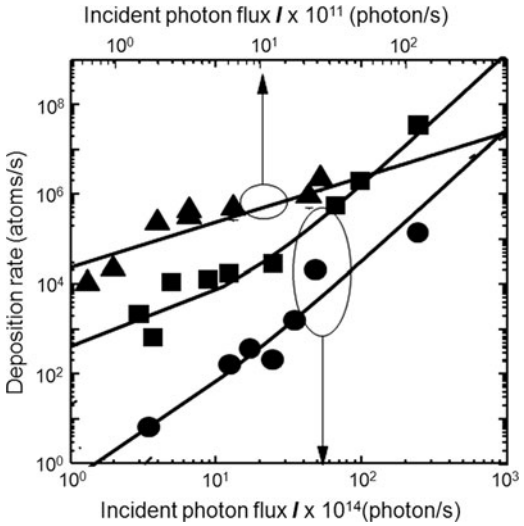

Fig. 1.23 The relation between the photon flux I of the light incident on the fiber probe tip and the deposition rate R of the Zn nanometric particles. *Closed triangles*, *squares*, and *circles* represent the results obtained by using the ultraviolet, blue, and red light sources, as in the cases of Fig. 1.22a, b, and c, respectively

This relation was confirmed experimentally by measuring the values of b/a and c/b, which were found to be on the order of 10^{-15}, thus supporting the validity of the theory based on the DP–CP picture [50].

On the basis of the dressed photon theory and the important role of electric dipole-forbidden molecular vibrational excitations, recent theoretical studies have proposed a simple model to describe atom or atom-cluster desorption due to the dressed photons from a nanometric particle deposited on a substrate [49]. Assuming an anharmonic potential for each atomic binding, an effective atom-nanodot potential was evaluated to determine the desorption energy and the stabilized dot size. The model shows that electric dipole-forbidden molecular vibrational excitations play an important role in the phonon-assisted process, which could potentially lead to a novel fabrication method, in addition to controlling the size and position of nanostructures [51].

1.5.2 Photolithography

The phonon-assisted process can be applied also to photolithography to pattern widely available commercial photoresists by using a visible light source even though such photoresists are sensitive only to UV light. To confirm this patterning ability, a film of commercial photoresist (OFPR) was coated on a substrate, and a photomask having a sub-wavelength sized aperture was mounted on it, as illustrated in Fig. 1.24a. Applying visible light to the photomask, low-intensity propagating light passes through aperture. However, the photoresist was not patterned by this propagating light because it is sensitive only to the UV propagating light. In contrast, a DP–CP is generated at the edge of the photoresist, and its energy is transferred to

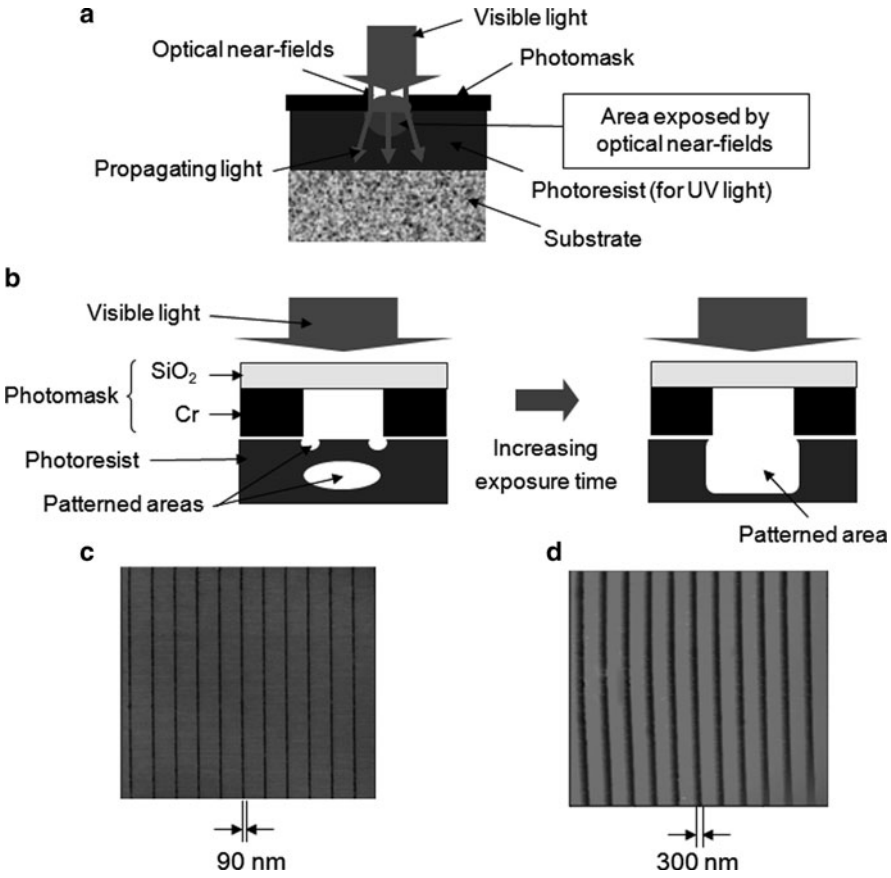

Fig. 1.24 Photolithography by phonon-assisted process. (**a**) Experimental set up. (**b**) Dependence of the cross-sectional profiles of the patterned photoresist areas on the exposure time. (**c**) and (**d**) are AFM images of the OFPR photoresist patterned by visible and UV light, respectively

the photoresist, by which the photoresist is activated and patterned by the phonon-assisted process [52]. From a theoretical analysis, it was found that the DP–CP was transferred not only to the surface of the photoresist but also to its inner part, by which these two parts of the photoresist could be effectively patterned with a short exposure time (Fig. 1.24b). By increasing the exposure time, the volumes of these patterns increased, and finally with an exposure time longer than a threshold value, they were connected with each other to form a pattern with a stable spatial profile that depended on the aperture size in the photomask. Figure 1.24c shows an AFM image of the linear pattern formed on the OFPR photoresist with an exposure time longer than the threshold. The linewidth of the fabricated pattern was as narrow as 90 nm, which is equivalent to the width of the aperture and is much narrower than the wavelength (550 nm) of the incident visible light. For comparison with the conventional photolithography based on the adiabatic process, the same OFPR

photoresist and the same photomask were used. However, they were illuminated by UV light to which the OFPR photoresist was sensitive. As shown in Fig. 1.24d, the resultant linewidth of the pattern was as wide as 300 nm, which is much broader than that of Fig. 1.24c. Such a broader linewidth was due to the diffraction of the propagating UV light passing through the aperture, to which the photoresist is sensitive. By comparing Fig. 1.24c, d, it is concluded that higher resolution was obtained by using a longer-wavelength light source, which is longer than the absorption band edge wavelength of the photoresist. This means that large, expensive, high-power-consumption, short-wavelength X-ray, EUV, and UV light sources are not required for phonon-assisted photolithography.

In addition to the high resolution obtained with a visible light source, this method based on the phonon-assisted process has several advantages, including:

(1) *Multiple exposure*. Figure 1.25a illustrates a UV-sensitive photoresist coated on a transparent substrate. A photomask was mounted on the photoresist, and visible light was applied from the back surface of the transparent substrate. After the visible light passed through the transparent substrate, it reached the surface of the photomask, resulting in generation of a DP–CP without activating the photoresist. The photomask was then patterned by this DP–CP due to the phonon-assisted process. An AFM image of the fabricated linear pattern is shown in Fig. 1.25b. Next, the photomask was mounted again on the same photoresist after rotating the direction of its linear axis by 90° (Fig. 1.25c). By applying the visible light again to generate the DP–CP on the photomask, the photoresist was patterned by the DP–CP without suffering any effects from the propagating visible light. The result is shown Fig. 1.25d, which shows a two-dimensional lattice structure formed by double-exposure through the linear-patterned photomask. By repeating these exposures, more complicated patterns can be realized. It should be pointed out that the contrast of this pattern (Fig. 1.25e) remained high even after multiple exposures because the photoresist was insensitive to the incident visible light.

(2) *Patterning of optically inactive films* [52]. As in the case of dissociating optically inactive $Zn(acac)_2$ molecules by the phonon-assisted PCVD (Fig. 1.22d), this method can pattern even optically inactive films. To confirm this, ZEP-520A, which has been popularly used as a resist film for electron beam (EB) lithography, was used as a test material. The surface of the film was spatially homogeneous and, thus, advantageous for realizing high resolution in EB lithography. However, it was optically inactive. For patterning by the present method, a ZEP-520A film was coated on a substrate, and a photomask was mounted on the film and illuminated by visible light (wavelength: 355 nm). The result is shown in Fig. 1.26, which shows that the pattern of the two-dimensional array of disks was transferred to the surface of the ZEP-520A film. This result confirms that the phonon-assisted lithography can pattern even an optically inactive film.

Based on the results outlined above, a prototype machine for producing commercial products has been constructed in collaboration with industry [53]. As shown in Fig. 1.27, it occupies an area as small as 1 m^2. It uses a conventional Xe lamp

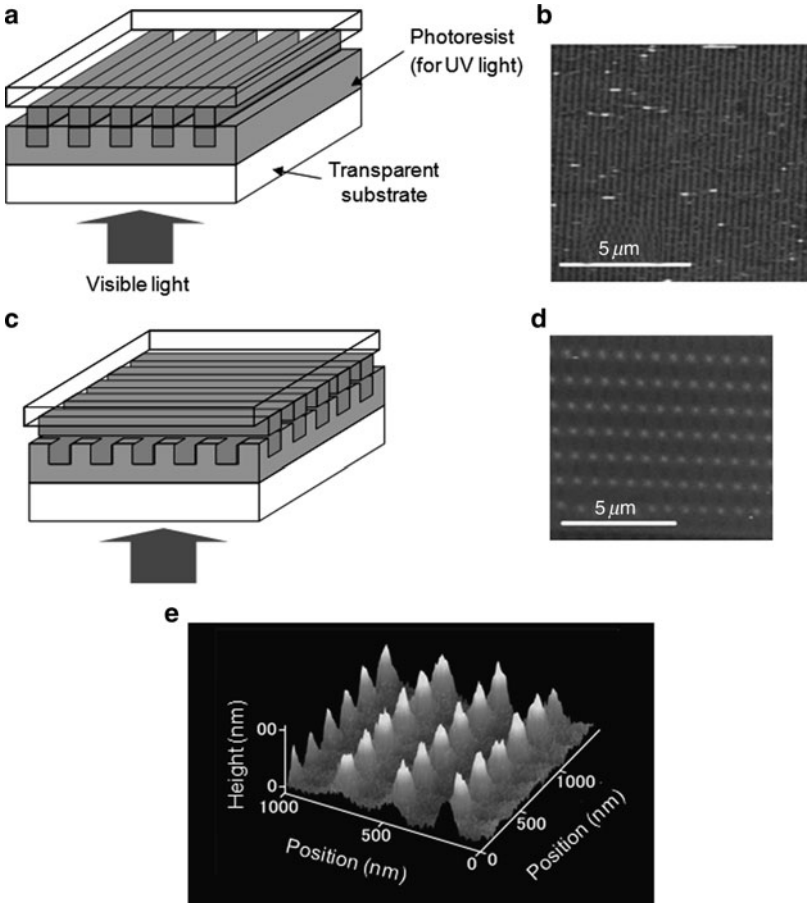

Fig. 1.25 Illustration of multiple exposure. (**a**) and (**b**) are the first-step exposure and AFM image of the patterned photoresist, respectively. (**c**), (**d**), and (**e**) are the second-step exposure, AFM images of the patterned photoresist, and a bird's eye view of (**d**), respectively

as a light source and is operated by computer-controlled robotics. A resolution of 20–50 nm is guaranteed for a substrate area of 50 mm × 60 mm. A wider patterned area is expected by employing a mechanical stepper system. A two-layer resist film is employed to fabricate a high-aspect-ratio pattern, a lubricant is coated to remove the photomask from the photoresist without damaging the photomask surface, and a novel photoresist material is composed to realize a sufficiently homogeneous film for high resolution. Although photomasks have been fabricated by electron beam lithography in the early stage of the present study, it has become possible to fabricate them by phonon-assisted photolithography.

It should be pointed out that a metallic photomask may sacrifice the resolution due to diffraction of the plasmonic wave. To solve this problem, the plasmonic wave

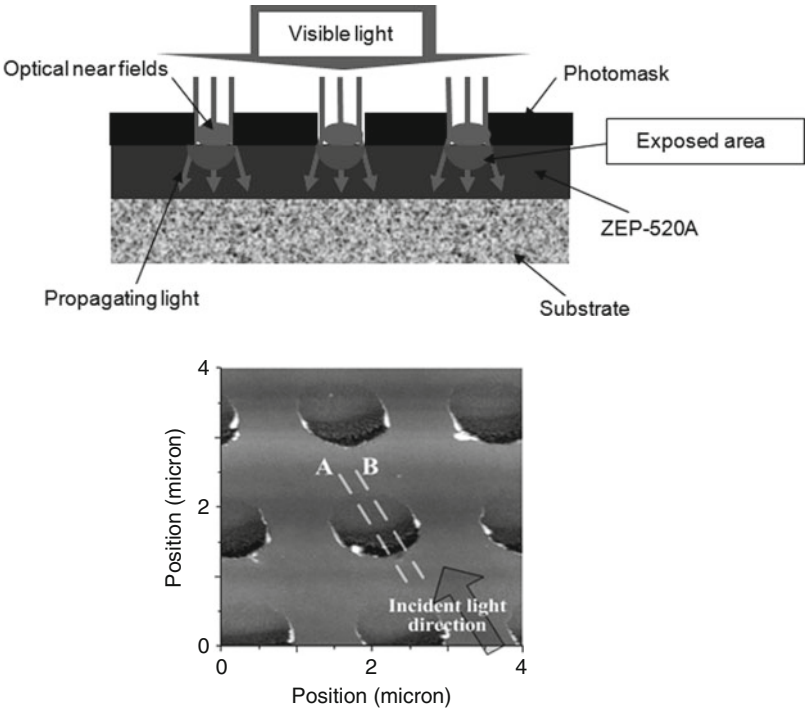

Fig. 1.26 Image of a two-dimensional array of disks patterned on an optically inactive ZP-520A film

on the photomask surface must be suppressed, for which it is advantageous to use Si as a photomask material.

Examples of the patterns fabricated by this machine are: a 40 nm-linewidth linear pattern (Fig. 1.28a), a high-aspect-ratio pattern (Fig. 1.28b), a pattern with a minimum linewidth of 22 nm realized by making high-resolution photoresist (Fig. 1.28c), two-dimensional arrays of rings and disks (Fig. 1.28d, e), and so on [53]. This machine has been made available for public use since April 2006. Examples of its use include the fabrication of a two-dimensional array of room-temperature operated nanophotonic NOT gates composed of InAs QDs (refer to Fig. 1.11), linear and curved Si optical waveguides, and so on.

Other examples of fabricated structures include diffraction gratings and Fresnel zone plates for soft X-rays with a wavelength of 0.5–1.0 nm. It should be pointed out that these devices were fabricated by using green light, whose wavelength is more than 500 times longer than that of soft X-rays. For the diffraction gratings, corrugations of 7,600 lines/mm were patterned on an Si substrate, as shown in Fig. 1.29a, which were coated with Mo/SiO_2 multilayer films. Figure 1.29b shows the evaluated diffraction efficiency, which is as high as 3% in the wavelength range of 0.5–1.0 nm. This is higher than that of a commercially available diffraction grating using the crystal lattice of KAP[54]. This high efficiency confirms the high resolution and

Fig. 1.27 Photograph of a prototype machine for a commercial product

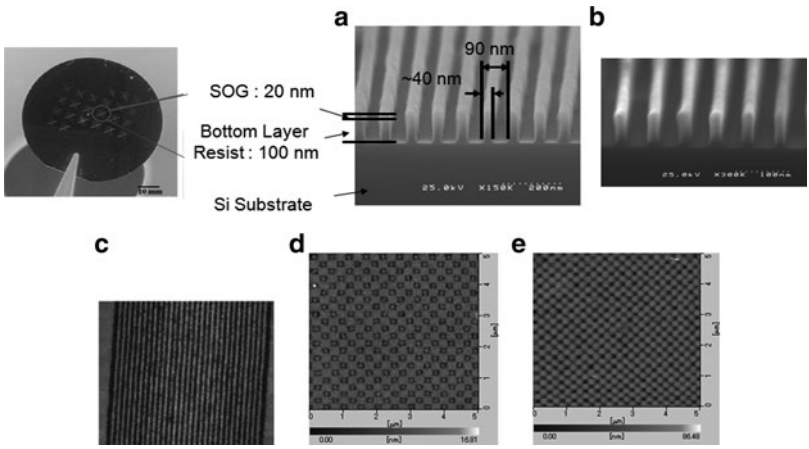

Fig. 1.28 Examples of patterns fabricated by the machine in Fig. 1.28. (**a**) A linear pattern of 40-nm width lines at 90-nm intervals. (**b**) High-aspect-ratio patterns with a half pitch of 32 nm. (**c**) The minimum linewidth (22 nm) of the linear patterns. (**d**) Two-dimensional array of 100-nm diameter rings. (**e**) Two-dimensional array of disks with 125-nm pitch

high reproducibility of the prototype lithography machine. For Fresnel zone plates, concentric circular patterns were fabricated on a Ta film [55]. Figure 1.30a shows a high-contrast SEM image of a fabricated Fresnel zone plate. The outer diameter, linewidth on the rim, and number of rings were 400 μm, 420 nm, and 230, respectively. The thickness of the Ta was 65 nm. The contrast of the pattern is plotted as a function of the order of the rings in Fig. 1.30b. This figure shows that the present phonon-assisted photolithography realized higher contrast than the conventional adiabatic photolithography, especially for rings of higher order.

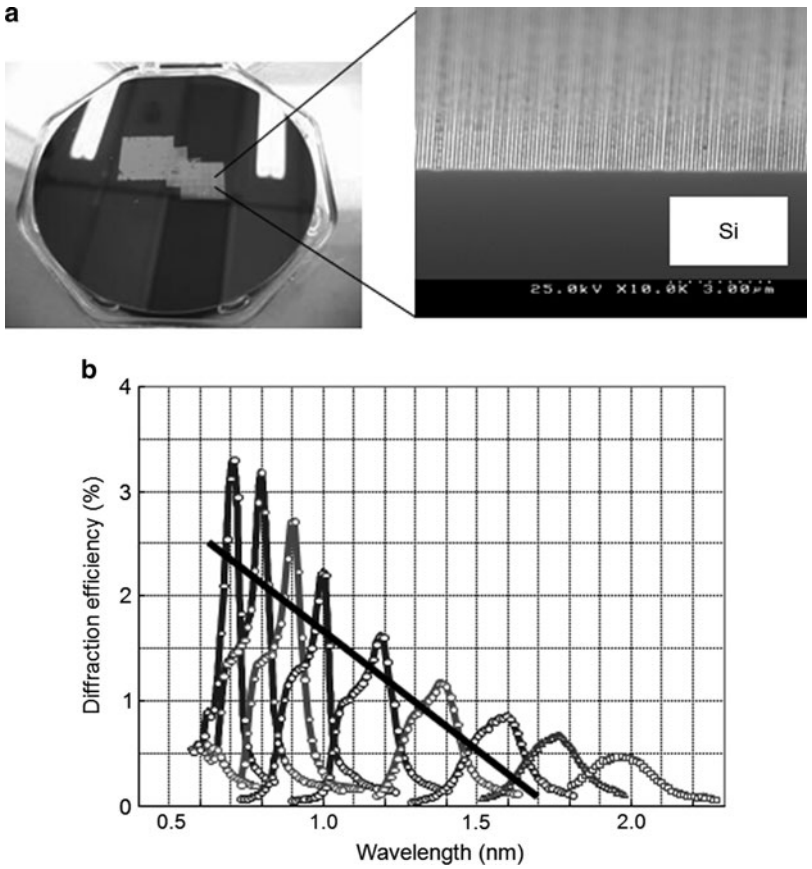

Fig. 1.29 Fabricated diffraction grating for soft X-rays. (**a**) SEM image. (**b**) Diffraction efficiency. The *black line* represents the efficiency of a commercially available one using the crystal lattice of KTP

A notable advantage of this method of fabricating soft X-ray optical devices is its mass-production capability. For example, Figure 1.31 shows a two-dimensional array of Fresnel zone plates prepared on the photomask. With an exposure of several minutes, these patterns were transferred to the photoresist, and thus, 49 Fresnel zone plates were simultaneously fabricated. This process demonstrates that the fabrication throughput is much higher than that of raster-scanned electron beam lithography, which has been conventionally used for fabricating Fresnel zone plates. This demonstrates that the dressed photon technology shows the possibility of mass-producing even devices for soft X-rays, from which novel applications are expected, such as portable soft X-ray fluorescence spectrometers for analyzing items of cultural heritage and security inspection systems.

Although the prototype machine of Fig. 1.27 is fully automatic and can be used to fabricate a variety of devices, a more compact and simple machine is sufficient

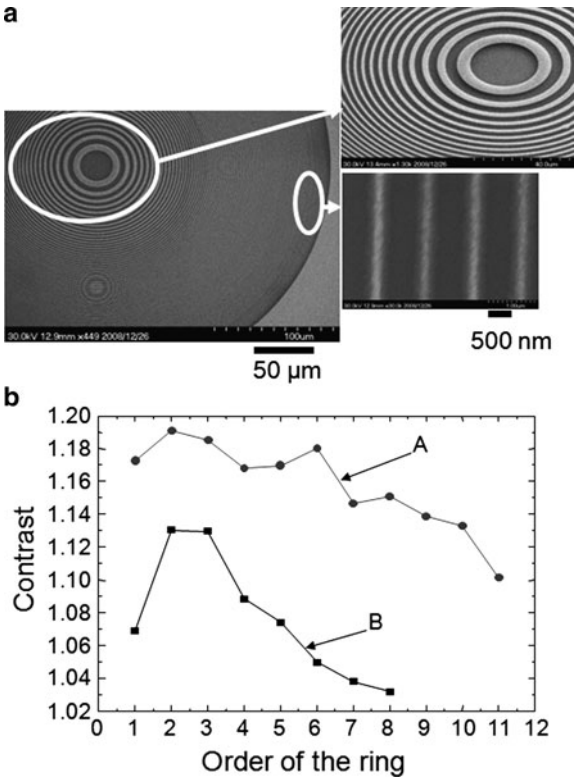

Fig. 1.30 Fabricated Fresnel zone plate. (**a**) SEM image. (**b**) Relation between the order of rings and the contrast. Zigzag lines A and B represent the contrasts of the Fresnel zone plates made by phonon-assisted and conventional adiabatic lithography, respectively

for the purpose of fabricating a limited species of devices. Figure 1.32 shows such a compact, desk-top machine with a footprint of only 0.03 m^2. A single light emitting diode (LED) emitting green light with a power of 30 mW and driven with input electrical power of 4.5 W was used as a light source. Even such a simple machine can fabricate a two-dimensional array of room-temperature operated nanophotonic NOT gates, linear and curved Si optical waveguides, diffraction gratings, and Fresnel zone plates for soft X-rays. Such machines have many benefits compared with conventional photolithography stepper systems, which are large and expensive and have high power consumption because they need short-wavelength light sources.

1.5.3 Self-Organized Smoothing

To demonstrate the phonon-assisted PCVD described in Sect. 1.5.1, a fiber probe was used for generating a DP–CP. Although arbitrary patterns can be drawn by raster-scanning the fiber probe, the throughput of the pattering is limited by its low scanning speed. Replacing the fiber probe with a photomask has drastically increased the throughput of phonon-assisted photolithography, which has enabled

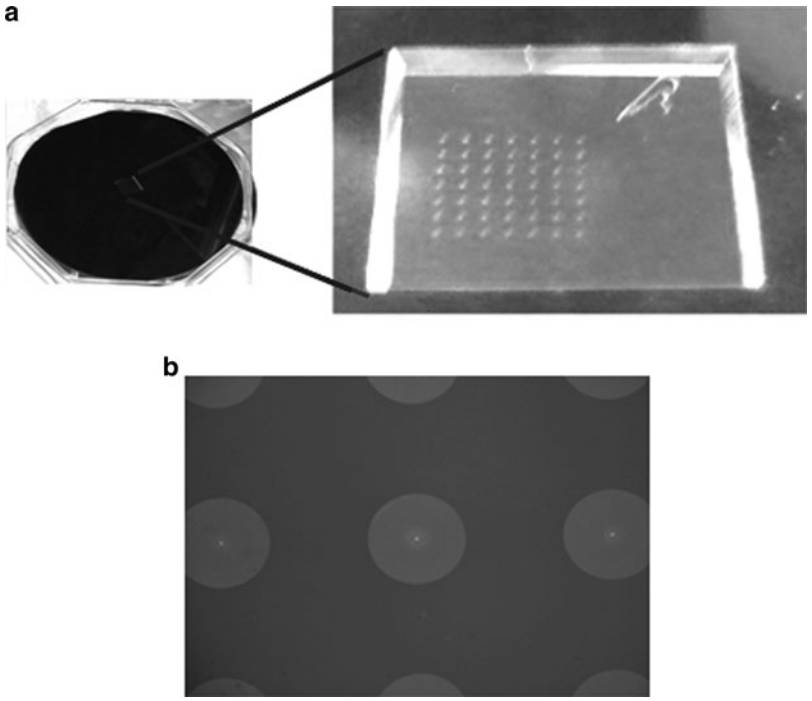

Fig. 1.31 Two-dimensional array of 7 × 7 Fresnel zone plates. (**a**) Patterns on the photomask. (**b**) Patterns transferred to the photoresist

the mass-production of devices for soft X-rays. Further increases in throughput are expected if the photomask can be removed entirely. Such maskless methods are reviewed in this section.

The key to these methods is to exploit the fact that optical near-fields, and thus DP–CPs, can always be generated on a nanometrically rough material surface when it is illuminated with light. Even if the surface is flat, DP-CSs are also generated at the parts at which the structure or component is nanometrically singular. The generated DP–CPs cause smoothing of locally rough parts or make the sizes of individual parts uniform. After they become flat or homogeneous, the smoothing or homogenizing stops automatically because the DP–CPs are no longer generated. Thus, they are called self-organized processes.

It should be noted that the methods reviewed below can be applied not only to a planar substrate but also to convex and concave substrates. They can also be applied to an inner wall surface of a cylinder if it can be illuminated by propagating light. Furthermore, they can be used for a variety of materials, such as glasses, crystals, ceramics, metals, plastics, and so on. Since a high optical power is not required, visible LEDs can be employed as low-power-consumption light sources.

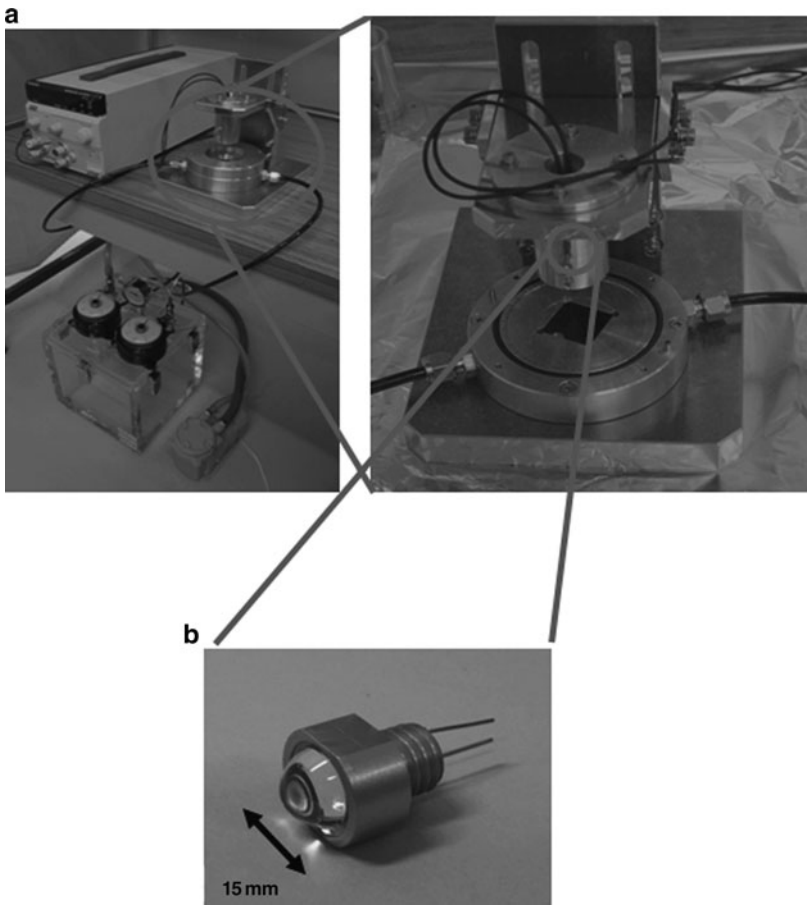

Fig. 1.32 A compact desk-top machine. (**a**) Photograph of the machine. (**b**) LED used as a light source

1.5.3.1 Repairing Surface Roughness

Surface roughness can be repaired by two methods, which are reviewed in this section

1. *Etching* [56]. Phonon-assisted photochemical etching was developed for smoothing the surface of glass, with the goal of fabricating high-quality mirrors for high-power, short-pulse laser systems. The experimental setup is shown in Fig. 1.33. A glass substrate with nanometric surface roughness is installed in a vacuum chamber filled with gaseous Cl_2 molecules. Although the absorption band edge wavelength of these molecules is 400 nm, green propagating light with a wavelength as long as 532 nm is used for photochemical etching. The Cl_2 molecules remain stable above the flat glass surface because of the absence

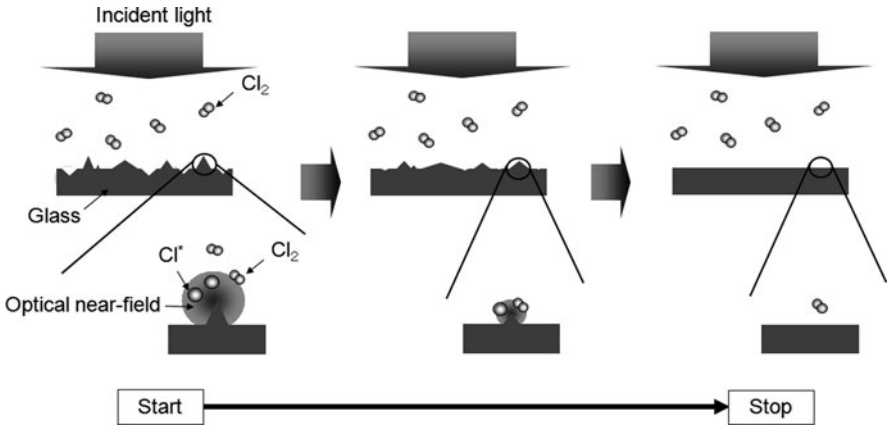

Fig. 1.33 Schematic explanation of phonon-assisted photochemical etching of a glass substrate surface

of DP–CPs. However, DP–CPs are generated at the tips of bumps on the illuminated rough surface, and by exchange of DP–CPs between the bumps and the Cl_2 molecules, the Cl_2 molecules are dissociated to produce radical Cl atoms, which etch the tips of the bumps. By this phonon-assisted process, the photochemical etching starts spontaneously to remove the bumps when the glass surface is illuminated with incident propagating light, and it stops spontaneously when the glass surface becomes so flat that DP–CPs are no longer generated. Thus, it is a self-organized method of smoothing the surface.

As shown in Fig. 1.34a, the magnitude of the roughness is represented by the quantity Ra, which decreased from 0.23 to 0.13 nm after 60 min of photochemical etching. This figure shows that the scratches, bumps, and digs formed in the process of preliminary mechano-chemical polishing were successfully removed by the phonon-assisted photochemical etching. Statistical analysis of the roughness quantitatively confirmed that the roughness was drastically removed after the photochemical etching (Fig. 1.34b)[57].

2. *Desorption* [58]. Phonon-assisted desorption was developed for smoothing the surface of transparent alumina (Al_2O_3), which is a hard polycrystalline ceramic, with the aim of fabricating low-loss gain media for ceramic lasers to be used in laser-driven spark plugs for the ignition systems in automobile engines [59]. It was expected that surface roughness, including the scratches formed in the preliminary grinding by diamond abrasive grains, would be repaired by sputtering Al_2O_3 particles and phonon-assisted desorption. An alumina substrate is placed in a vacuum chamber, and Al_2O_3 particles are deposited on the substrate by RF sputtering. In the case of conventional RF sputtering, the migration length of Al_2O_3 particles on the substrate surface depends on the Schwöbel barrier in the free energy and is very short at the ridges of scratches. This means that the deposition rate of the Al_2O_3 particles is higher at the ridges than at flat areas.

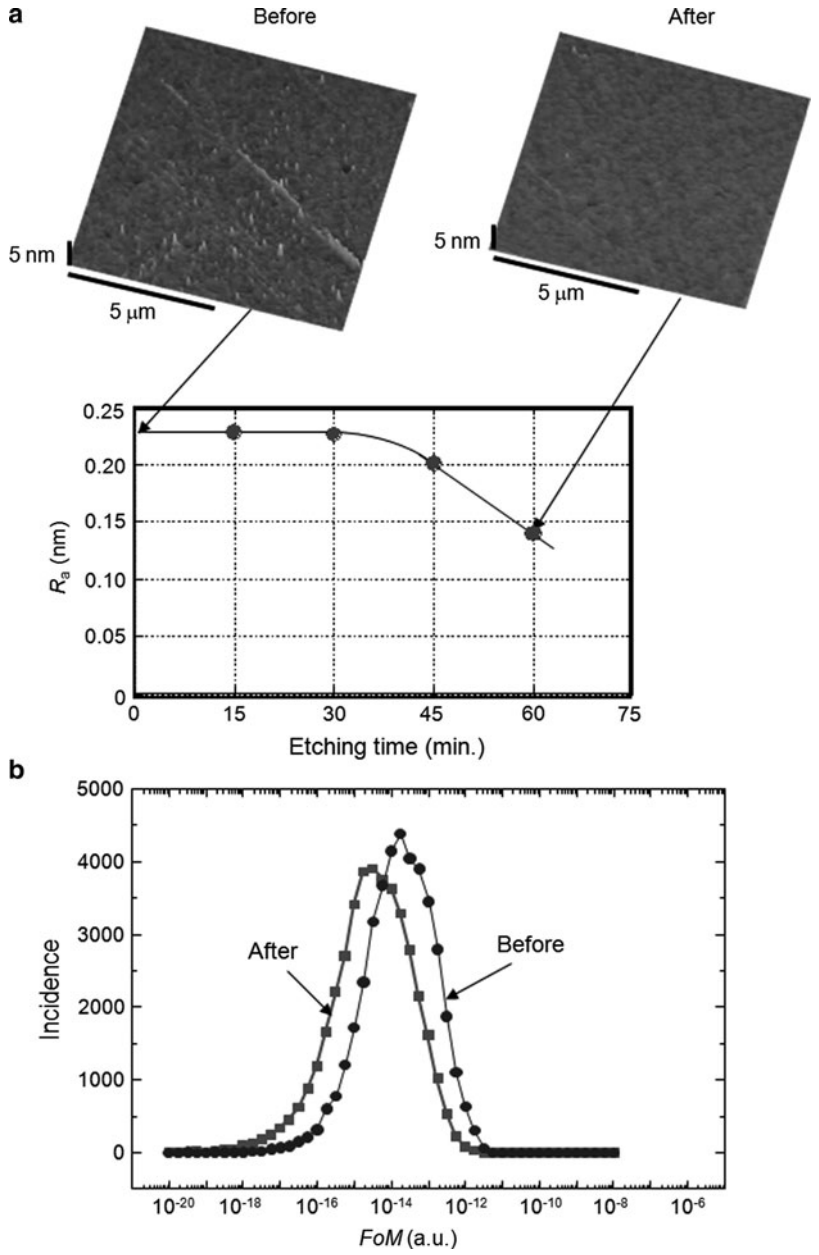

Fig. 1.34 Results of phonon-assisted photochemical etching of a glass substrate surface. (**a**) AFM images of the glass surfaces before and after the etching. Relation between the etching time and the surface roughness Ra is also shown. (**b**) Incidence pattern of the figure of merit, FoM, before and after the etching

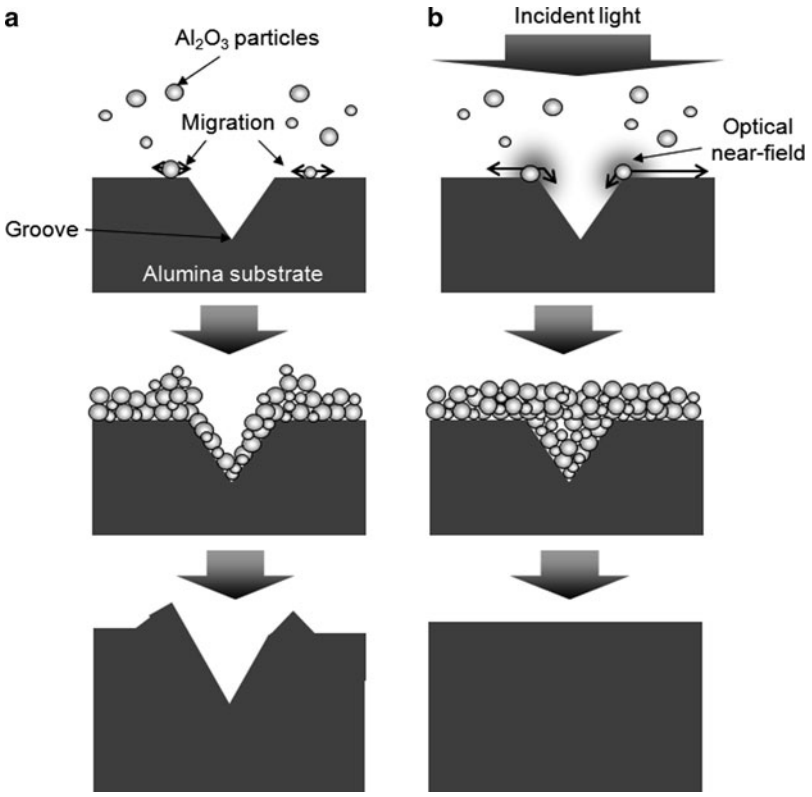

Fig. 1.35 Illustration of sputtering of Al_2O_3 particles on an alumina substrate surface (**a**) by conventional RF sputtering, and (**b**) by RF sputtering under visible light illumination

As a result of the difference in the deposition rate, Al_2O_3 particles are preferentially deposited on the ridges of scratches, as illustrated in Fig. 1.35a, making it impossible to repair the scratches. To repair them, the substrate is illuminated with visible light (400 mW cm^{-2} power density) whose wavelength (473 nm) is longer than that of the absorption band edge wavelength (260 nm) of the Al_2O_3 particles, as shown in Fig. 1.35b. By this illumination, DP–CPs are generated on the ridges of the scratches, which causes the Al_2O_3 particles to be activated, increasing the migration length, or which causes them to be desorbed from the ridge. On the other hand, on the flat areas and the slopes of the scratches, the Al_2O_3 particles are deposited with the same deposition rate as that of Fig. 1.35a because of the absence of DP–CPs. It should be pointed out that the DP–CPs are not generated at the bottom of the scratches because the substrate material around the bottom does not have nanometer-scale dimensions but is bulky, making it impossible to excite coherent phonons. By this phonon-assisted process, the deposition at the ridges is suppressed, whereas the bottoms of the scratches are filled by the Al_2O_3 particles, and finally, the scratches are repaired. It is a

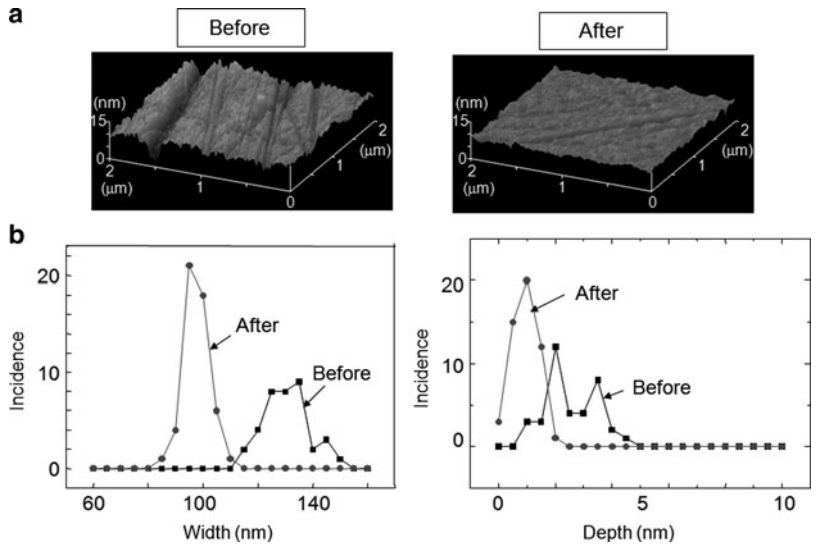

Fig. 1.36 Experimental results of the RF sputtering. (**a**) AFM images of the alumina substrate surface before and after the RF sputtering under visible light illumination. (**b**) The results of performing Hough transforms of the AFM images

self-organized method of smoothing the surface, as in case (1). Experimental results are shown in Fig. 1.36a, which shows a drastic change in the surface profile. Statistical analysis using a Hough transform revealed that the average width of the scratches decreased from 128 to 92 nm using this method. The average depth decreased from 3 to 1 nm, as shown in Fig. 1.36b.

1.5.3.2 Homogenizing Mole-Fraction Ratio

It should be pointed out that the DP–CPs are always generated at parts at which the structure or component of a substrate is locally singular even though its surface is morphologically flat. By exploiting this, the spatial distribution of the mole-fraction ratio, x, of indium (In) in an $In_xGa_{1-x}N$ film was homogenized by phonon-assisted desorption in a self-organized manner [60]. The motivation for this homogenization is to increase the color-rendering index of an $In_xGa_{1-x}N$ LED by controlling the spectral profile of the emitted light for applications to high-quality lighting, displays, and so on. It is possible to control this index because the emission wavelength, λ_e, increases from 400 nm to 1.50 μm by increasing x from 0 to 1, as a result of the decrease in the bandgap energy, E_g, from 3.10 to 0.83 eV. The principle of this homogenization is illustrated in Fig. 1.37. While the TEI, TMG, and NH_3 source gases are supplied for doping In, Ga, and N, respectively, in the $In_xGa_{1-x}N$ on the substrate, the film surface is illuminated with visible light. Due to this illumination, DP–CPs are generated on the film surface with a spatial profile that depends

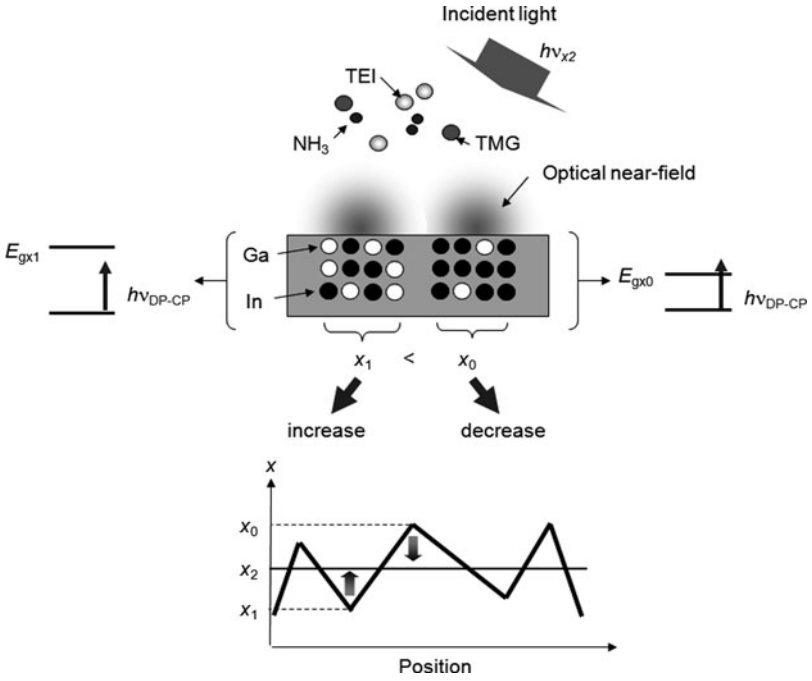

Fig. 1.37 Schematic explanation of homogenizing mole-fraction ratio x of $In_xGa_{1-x}N$ by phonon-assisted desorption

on the local singularities, i.e., on the mole-fraction ratio, x. In an area of larger mole-fraction ratio x_0 and bandgap energy E_{g0} lower than the energy $h\nu_{DP-CP}$ of the DP–CPs, the $In_xGa_{1-x}N$ film absorbs the DP–CP energy and transfers it to the doped In for desorption. As a result, the mole-fraction ratio x_0 decreases. On the other hand, in an area of lower mole-fraction ratio x_1 and bandgap energy E_{g1} higher than the energy $h\nu_{DP-CP}$, the $In_xGa_{1-x}N$ film does not absorb the DP–CP energy, and thus, the In can be steadily doped into the substrate without desorption. As a result, the mole-fraction ratio x_1 increases. The decrease and increase continue until the bandgap energies E_{g0} and E_{g1} reach $h\nu_{DP-CP}$. Finally, both the mole-fraction ratios x_0 and x_1 reach a value x_{DP-CP}, which is determined by $h\nu_{DP-CP}$. This means that the mole-fraction ratio can be spatially homogenized in a self-organized manner. Further, the photon energy of the incident light can determine the value x_{DP-CP} of the homogenized mole-fraction ratio and the wavelength of the light emitted from the $In_xGa_{1-x}N$ film.

For experimental confirmation of this effect, room-temperature PCVD was employed to grow an $In_xGa_{1-x}N$ film on a sapphire substrate [61] while visible light was made incident on the film surface for desorbing In. Figure 1.38 shows the spectral profiles of the photoluminescence emitted from the $In_xGa_{1-x}N$ film grown in this way. In Fig. 1.38a, spectral narrowing is seen in the area of the photon energy lower than that of the incident light ($h\nu_{FP} = 2.71$ eV; wavelength = 457 nm;

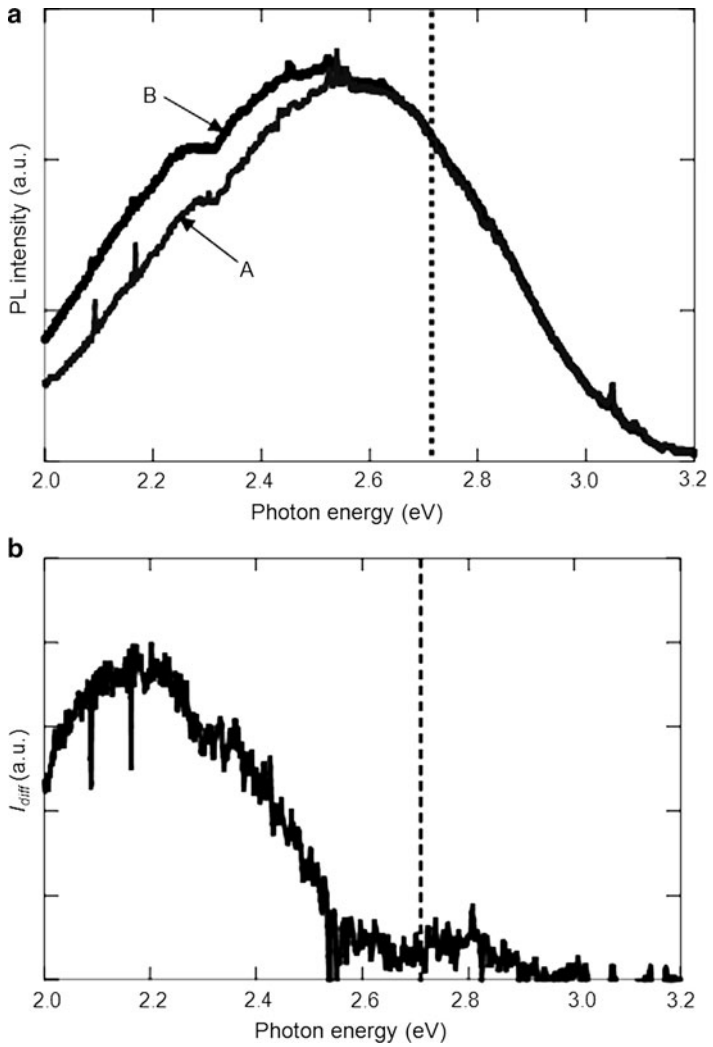

Fig. 1.38 Spectral profiles of the photoluminescence emitted from the $In_xGa_{1-x}N$ film. (**a**) Curves A and B represent the spectra from the film grown by the present method and by the conventional method, respectively. (**b**) Difference of spectral intensities of the curves A and B in (**a**). The *broken vertical lines* in these figures represent the photon energy of the incident light (= 2.71 eV)

power = 200 mW). Furthermore, the differential spectral intensity monotonically decreases with the increase of the photon energy (Fig. 1.38b). These features represent the results of homogenization of the mole-fraction ratio by phonon-assisted desorption.

1.6 Nanophotonic Energy Conversion

Noting that (1.4) represents energy up-conversion from the free photon to the DP–CP, this section reviews novel methods of optical/optical energy conversion and optical/electrical energy conversion.

1.6.1 Optical/Optical Energy Up-Conversion

To confirm the optical energy up-conversion, powdery grains of DCM organic dye molecules were placed in a quartz container and used as a test material [62]. Although the absorption band-edge wavelength of the DCM is as short as 670 nm, the grains were illuminated by near infrared light of 805-nm wavelength, as illustrated in Fig. 1.39a. This illumination generated the DP–CPs at the edges of grains, which were then exchanged between the adjacent grains. As a result of this exchange, an electron in the adjacent grain was excited by a phonon-assisted process, and then, it emitted light whose photon energy was higher than that of the incident light due to the contribution of the phonon energy. Figure 1.39b shows the spot of red light emitted from the grains as a result of the frequency up-conversion. Figure 1.39c shows an optical microscopic image of the 650-nm wavelength spectral component of the emitted light. The spatial distribution of the emitted light intensity in this figure is inhomogeneous because the light was emitted selectively from the edges of the grains, which demonstrates the phonon-assisted process due to the DP–CPs generated at the edges of the grains. For comparison, Fig. 1.39d shows an optical microscopic image of conventional 650-nm fluorescence, which is emitted as a result of the frequency down-conversion under illumination with 402-nm wavelength light. The spatial distribution of the fluorescence intensity is homogeneous, in contrast to that of Fig. 1.39c.

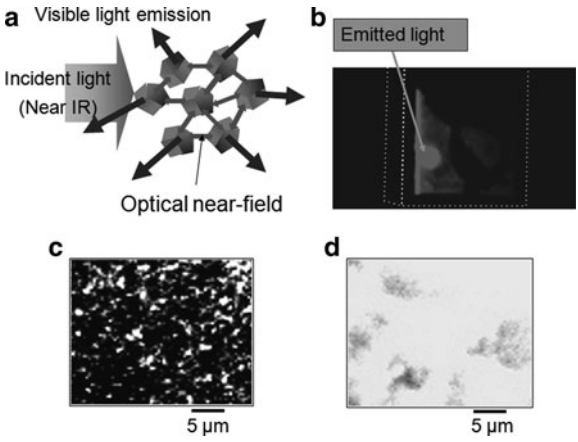

Fig. 1.39 Frequency up-converted light emission from powdery grains of DCM organic dye molecules. (**a**) Illustration of the emission mechanism. (**b**) Light spots emitted from the grains placed in a quartz container. (**c**) Optical microscopic image of the frequency up-converted light (wavelength, 650 nm). (**d**) Optical microscopic image of conventional fluorescence

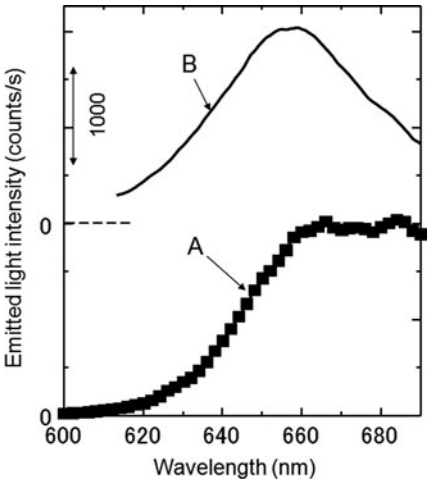

Fig. 1.40 Spectral profiles of the frequency up-converted light. Curve A is the spectrum obtained by applying near-infrared light with a wavelength of 805 nm. Curve B is the conventional fluorescence spectrum

The curve A in Fig. 1.40 shows the spectral profile of the frequency up-converted light measured by applying near infrared light with a wavelength of 805 nm. The curve B shows the conventional fluorescence spectral profile excited by the 402-nm wavelength light. Spectral profiles in the wavelength range shorter than 660 nm show similar curves, which means that the up-converted light is emitted from the electrons in the same excited state as that involved in emitting the fluorescent light. Experimental results of the temporal behaviors of the frequency up-converted light intensity were least squares-fitted to an exponentially decaying function with two decay constants, 0.45 and 1.37 ns. This fitting confirmed again that the up-converted photon was emitted from the electron of the same excited state as that for the fluorescence. However, the spectral intensity of curve A in the longer wavelength range is as high as that of its spectral peak, which means that the longer wavelength light is emitted from a long-lived electronic excited state to which the electron relaxes after the phonon-assisted excitation.

Figure 1.41a shows the relation between the incident light intensity I used for excitation and the frequency up-converted light intensity I_{uc} emitted from the powdery grains of the DCM organic dye molecules. Experimental results are presented for the wavelength components of 650 and 690 nm, to which the curve

$$I_{\mathrm{uc}} = aI + bI^2 \tag{1.8}$$

was least-squares fitted. The fitted results are represented by solid curves. The fitted curves show that the frequency up-conversion is due to the two-step excitation by the DP–CP, as described in the following (Fig. 1.41b); here, $|E_\alpha; el\rangle$ and $\left|E_\beta; vib\right\rangle$ represent molecular electronic and vibration (phonon) states, respectively, and E_α ($\alpha = g, ex$) and E_β ($\beta = i, a, b, thermal, em$) represent the molecular electronic and vibrational energies, respectively:

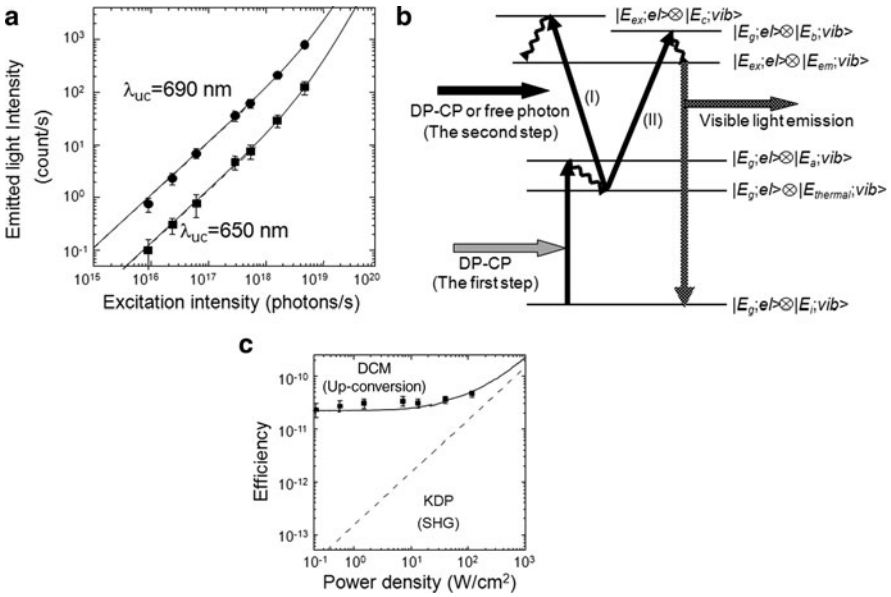

Fig. 1.41 (**a**) Relation between the incident light intensity and the frequency up-converted light intensity. (**b**) Illustration of the two-step excitation and subsequent light emission. (**c**) Efficiency of the frequency up-conversion as a function of the incident light power density. For comparison, the efficiency of the second harmonic generation from a KDP crystal is also shown

1. *First-step excitation.* After the excitation light generates a DP–CP at the edge of the DCM grain, the DP–CP induces the transition from $\left|E_g;el\right\rangle \otimes |E_i;vib\rangle$ to $\left|E_g;el\right\rangle \otimes |E_a;vib\rangle$ due to the phonon-assisted excitation.
2. *Second-step excitation.* After the first-step excitation, the excited coherent phonon relaxes to the thermal equilibrium state $\left|E_g;el\right\rangle \otimes |E_{\text{thermal}};vib\rangle$ with a relaxation rate of about 100 meV ps^{-1}. If the energy of the re-distributed phonon in the $\left|E_g;el\right\rangle \otimes |E_{\text{thermal}};vib\rangle$ state exceeds the energy difference of 0.34 eV between the electronic excited state in a molecule and the photon energy of the incident light, the excitation occurs via two possible routes. One route (I) is from $\left|E_g;el\right\rangle \otimes |E_{\text{thermal}};vib\rangle$ to $|E_{\text{ex}};el\rangle \otimes |E_c;vib\rangle$ due to the conventional adiabatic photo-excited process. The other (II) is from $\left|E_g;el\right\rangle \otimes |E_{\text{thermal}};vib\rangle$ to $\left|E_g;el\right\rangle \otimes |E_b;vib\rangle$. After the excitation (I) or (II), both $|E_{\text{ex}};el\rangle \otimes |E_c;vib\rangle$ and $\left|E_g;el\right\rangle \otimes |E_b;vib\rangle$ relax to $|E_{\text{ex}};el\rangle \otimes |E_{\text{em}};vib\rangle$ due to cooling or the coupling of the phonon and electronic states, respectively.

After the two-step transition described above, visible light is emitted by the transition from $|E_{\text{ex}};el\rangle \otimes |E_{\text{em}};vib\rangle$ to $\left|E_g;el\right\rangle \otimes |E_i;vib\rangle$. Since the excitation (I) is a conventional adiabatic process, its probability of occurrence is more than 10^6 times that of the first-step excitation. Furthermore, the probability of visible light emission by the infrared excitation is governed only by the phonon-assisted excitation of the first step because the second-step transition easily saturates. This is the origin

of the linear intensity dependence (the first term of (1.8)). Because the excitation (II) is phonon-assisted, its probability of occurrence is equal to that of the first-step transition. This is the origin of the squared dependence (the second term of (1.8)). As a whole, the relation between I and I_{uc} is represented by (1.8) [63].

The efficiency of the frequency up-conversion is plotted in Fig. 1.41c as a function of the incident light power density. For comparison, this figure also shows the efficiency of conventional second harmonic generation from a popular KDP crystal, which has the same optical thickness as that of the powdery grains of DCM organic dye molecules placed in the quartz container. It is easily found that the efficiency of the frequency up-conversion is more than 100 times higher than that of the second harmonic generation for an incident light power density lower than 1 W cm^{-2}. By increasing the incident light power density, the second-step excitation of the phonon-assisted process becomes dominant, and thus, the conversion efficiency increases in proportion to the incident light power density due to the second term of (1.8). This term maintains the conversion efficiency higher than that of the second harmonic generation even at higher incident power density, by which it is confirmed that the efficiency of this frequency up-conversion is sufficiently high.

In addition to the two-step excitation due to the two degenerate DP–CPs generated by a single type of incident light as was reviewed above, it has been found that non-degenerate two-step excitation can also emit higher-frequency light by using two mutually independent light beams with different wavelengths [64]. Using this non-degenerate two-step excitation with high conversion efficiency, a novel system for optical pulse shape measurement has been developed: An optical pulse to be measured is incident on the powdery grains of the organic dye molecules. Simultaneously, a reference optical pulse with sufficiently short pulse duration is also incident on the grains with a variable time delay. Due to these two non-degenerate optical pulses, the grains are excited by the two-step phonon-assisted process. By measuring the emitted light intensity with a conventional visible photo-detector as a function of the time delay of the reference optical pulse incidence, the optical pulse shape to be measured can be acquired. Several experiments using DCM dye molecules have confirmed that the optical pulse shape of the 800-nm wavelength was measured with a temporal resolution of 0.8 ps, which was limited by the lifetime of the intermediate state involved in the two-step excitation. It should be noted that the measured optical pulse shape has low jitter because the present measurement system employs only an optical process, unlike the conventional streak-camera system employing an electro-optical process. By using other commercially available dye molecules, the measurable wavelength range can be extended to 1.3–1.55 μm with a temporal resolution of 0.8 ps, which enables optical pulse shape measurement for optical fiber transmission systems.

Instead of the powdery grains of organic dye molecules, a variety of materials can be used for optical frequency up-conversion so long as the DP–CPs are efficiently generated on their surfaces.

1.6.2 Optical/Electrical Energy Up-Conversion

The DP–CP can be used to convert optical energy to electrical energy with frequency up-conversion. This section reviews two examples.

1. *Selective photocurrent generation in the transparent wavelength range of an organic thin film photovoltaic device* [65]. Frequency up-conversion can extend the photodetection bandwidth of a photovoltaic device. For confirming this, a poly(3-hexylthiophene) (P3HT) organic thin film was used as a p-type semiconductor, whereas a ZnO film was used as an n-type semiconductor. They were sandwiched by a transparent ITO film and an Ag film to be used as electrodes. It should be noted that no photocurrent is generated from this device if it is illuminated by light whose wavelength is longer than the absorption band-edge wavelength λ_c (=570 nm), which is governed by the bandgap energy E_g of the P3HT.

For generating a DP–CP effectively, a novel method is employed to fabricate a nanometric structure on an Ag film. That is, while the Ag is deposited by RF-sputtering, the surface of the Ag film is illuminated with light whose wavelength is longer than the absorption band-edge wavelength of the P3HT. As a result of this illumination, an intrinsic nanometric structure is spontaneously formed on the surface of the Ag film due to the phonon-assisted process, as has been experimentally demonstrated previously [51]. The present device is operated by using this Ag thin film as an electrode. Utilizing the phonon-assisted process induced by the DP–CP, the present method expands the working wavelength range of this device beyond the one limited by E_g even though the semiconductor materials remain untreated. Furthermore, a wavelength-selective feature of photocurrent generation is realized by controlling the morphology of the metallic electrode surface.

It is possible to excite electrons by a two-step phonon-assisted process for creating electron–hole pair (Fig. 1.42): The first step is the transition from the initial state in the HOMO ($|E_g; el\rangle \otimes |E_{\mathrm{ex,thermal}}; phonon\rangle$) to the intermediate state ($|E_g; el\rangle \otimes |E_{\mathrm{ex}}; phonon\rangle$) by the DP–CP. Here, $|E_g; el\rangle$ represents the ground state of the electron, $|E_{\mathrm{ex,thermal}}; phonon\rangle$ represents the thermal equilibrium state of a phonon whose energy is determined by the lattice temperature, and $|E_{\mathrm{ex}}; phonon\rangle$ represents the excited state of a phonon whose energy depends on the energy of the DP–CP. The DP–CP is indispensable for this transition because it is electric dipole-forbidden.

The second step is the transition from the intermediate state to the final excited state in the LUMO ($|E_{\mathrm{ex}}; el\rangle \otimes |E_{\mathrm{ex}'}; phonon\rangle$) by the DP–CP or the free photon (conventional propagating light). Here, $|E_{\mathrm{ex}}; el\rangle$) represents the excited state of the electron, and $|E_{\mathrm{ex}'}; phonon\rangle$ represents the excited state of a phonon whose energy depends on the photon energy used for the transition. Since this transition is electric dipole-allowed, it can be brought about not only by the DP–CP but also by the free photon. After this transition, the excited phonon relaxes to the thermal equilibrium state. $|E_{\mathrm{ex}',\mathrm{thermal}}; phonon\rangle$

The phonon-assisted process is used twice: once for efficient photocurrent generation in the wavelength range beyond the one limited by E_g, and once for fabricating a metallic electrode for the device, in which the morphology of the electrode surface

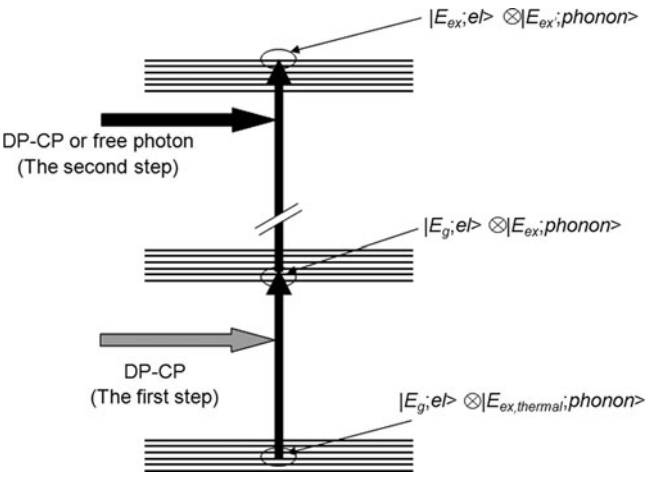

Fig. 1.42 Illustration of the two-step phonon-assisted process

can be controlled in a self-organized manner so that the phonon-assisted process is efficiently induced for photocurrent generation. For this self-organized control, Ag is deposited by RF-sputtering under light illumination on the previously deposited Ag thin film while the P3HT/ZnO pn-junction is reversely biased with a DC voltage V_b. Here, V_b was fixed to -1.5 V, and the wavelength λ_0 of the incident light was 660 nm, which is longer than λ_c of the P3HT. It is expected that this deposition with light illumination controls the morphology of the Ag film as a result of the phonon-assisted process induced by the DP–CP. When the Ag film with this controlled morphology is used as an electrode of the device, it is also expected that a conspicuous phonon-assisted process will be induced for photocurrent generation.

The mechanism of controlling the morphology is:

Step 1: Under light illumination, an optical near-field is generated on the Ag surface. This optical near-field excites a coherent phonon at the pn-junction, resulting in generation of a DP–CP. By the two-step phonon-assisted process, electrons can be excited to create electron–hole pairs at the pn-junction even though the photon energy of the incident light is lower than E_g.

Step 2: The created electron–hole pairs disappear because the electrons and positive holes are separated from each other due to the electric field of the reverse bias voltage. As a result, the positive holes are injected into the deposited Ag.

Step 3: Since the sputtered Ag is positively ionized due to the transmission of the Ag through the argon plasma or due to the collision of the argon plasma with the Ag-target used for RF-sputtering, these positively ionized Ag particles are repulsed from the area of the positively charged Ag film in which the positive holes have been injected in the manner described in Step 2. This

means that subsequent deposition of Ag is suppressed in the area in which the DP–CP is generated efficiently. As a result, a unique granular Ag film is formed, which depends on the spatial distribution of the DP–CP energy. This granular Ag film grows in a self-assembled manner with increasing RF-sputtering time, resulting in the formation of a unique morphology.

By using this morphology-controlled Ag film as an electrode of the device and by applying the incident light from the rear surface of the sapphire substrate, it is expected that the DP–CP can be efficiently generated on the electrode. Thus, electron–hole pairs can be created efficiently by the phonon-assisted process if the photovoltaic device is illuminated by light with the same wavelength λ_0 as the one used for controlling the morphology of the Ag film. On the other hand, if it is illuminated by light of a different wavelength λ_1, the efficiency of the electron–hole pair creation should be lower because the spatial profile and the photon energy of the generated DP–CP are different from those in the case of using λ_0 for controlling the morphology. Thus, this device should exhibit wavelength-selectivity in the photocurrent generation, which should take a maximum at the wavelength λ_0. Furthermore, since this wavelength is longer than λ_c, the working wavelength becomes longer than that limited by E_g.

Ag was deposited on the previously fabricated Ag film by RF sputtering. Device 1 was fabricated without applying V_b and the incident light power P, which was used as a reference to evaluate the performance of Device 2. For Device 2, V_b and P were -1.5 V and 70 mW, respectively. Figure 1.43a, b show SEM images of the Ag film surfaces of Devices 1 and 2. By comparing them, it is clear that the Ag surface of Device 2 (Fig. 1.43b) was very rough, with larger grains than those of Device 1 (Fig. 1.43a). The average and standard deviation of the diameters of the grains of Fig. 1.43b were 86 and 32 nm, respectively. The sum of the thicknesses of the Ag and P3HT was estimated to be less than 70 nm. Therefore, it is expected that the DP–CP generated on the Ag grains of Fig. 1.43b can extend to the pn-junction because the average diameters of these grains were 90 and 86 nm, respectively. As a result, it is expected that this DP–CP efficiently creates electron–hole pair at the pn-junction by the phonon-assisted process.

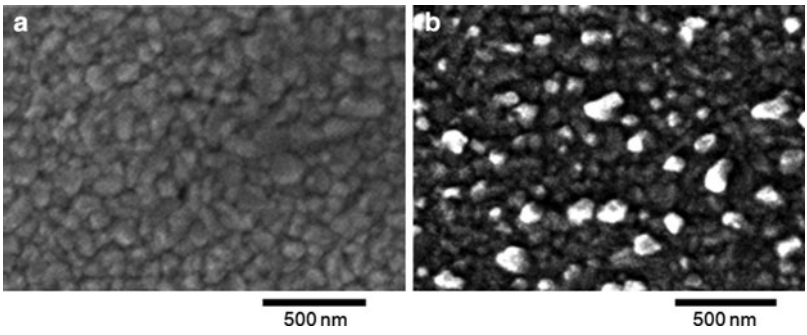

Fig. 1.43 SEM images of Ag film surfaces. (**a**) and (**b**) are for Devices 1 and 2, respectively

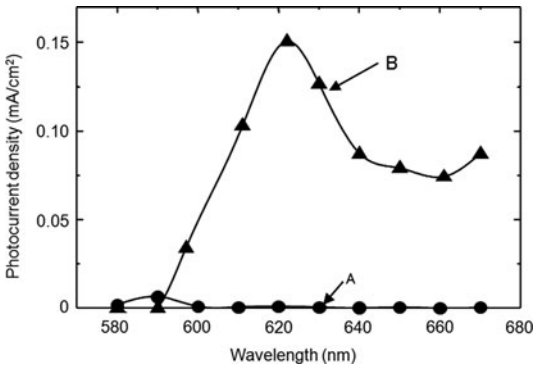

Fig. 1.44 Dependence of the generated photocurrent densities on the wavelength of the incident light. Curves A and B are for Devices 1 and 2, respectively

The detailed wavelength dependences of the photocurrent generation in the longer wavelength range beyond E_g of P3HT were evaluated, and the experimental results are shown in Fig. 1.44 for the wavelength range 580 nm $\leq \lambda_i \leq$ 670 nm. A linear relation between the incident light power and the generated photocurrent density was confirmed by preliminary experiments by applying low-power incident light (0.02–20 mW, corresponding to a power density of 2.5 mW cm^{-2} to 2.5 W cm^{-2}). This linear relation was attributed to the fact that the rate of creating electron–hole pairs was governed only by the electric dipole-forbidden transition of the first-step excitation under low-power-density excitation. The creation rate by the second-step excitation was sufficiently high because of the electric dipole-allowed transition. Based on this linear relation, the incident light power density was fixed to 125 mW cm^{-2} (1 mW optical power) for photocurrent density measurements. The photocurrent density from Device 1 was also very low, but it is shown by curve A as a reference.

Curve B represents the measured photocurrent densities from Device 2, generated by incident light with wavelengths up to $\lambda_i = 670$ nm, which clearly demonstrates the extension of the working wavelength range beyond that limited by E_g of P3HT. This curve also indicates the possibility of photocurrent generation even in the wavelength range longer than 670 nm. The photocurrent of curve B was the highest at $\lambda_{ip} = 620$ nm. Thus, Device 2 is effectively a wavelength-selective photovoltaic device for incident light with a wavelength beyond that limited by E_g. This wavelength λ_{ip} (= 620 nm) is 40 nm shorter than λ_0 (= 660 nm) used for controlling the morphology of the Ag film. This difference is attributed to the DC Stark effect induced by the reverse bias voltage V_b (= −1.5 V) applied in the process of controlling the morphology of the Ag film. The photocurrent density was 0.15 mW cm^{-2} at the peak of curve B ($\lambda_{ip} = 620$ nm), which corresponds to a quantum efficiency of 0.24% because the incident light power density was 125 mW cm^{-2}. This efficiency is as high as that of a conventional hetero-junction photovoltaic device using P3HT [66]. However, it should be pointed out that Device 2 realized such high quantum efficiency even for wavelengths longer than the one limited by E_g of P3HT.

It is expected that this method can be applied not only to P3HT but also to other organic and inorganic semiconductors because the phonon-assisted process was induced merely by controlling the morphology of the electrode while the semiconductor materials remained untreated. Higher efficiency can be expected by fine adjustment of the reverse bias voltage, light power, and wavelength used for controlling the morphology.

(2) *Extending the detection bandwidth of a GaN-MSM photodetector* [67]. A conventional metal–semiconductor–metal (MSM) photodetector, composed of two metallic electrodes and GaN, does not have any detection sensitivity for incident light with a wavelength longer than the absorption band-edge wavelength λ_c(=360 nm) of GaN. However, by sharpening the edges of the metallic electrodes, the incident light can generate a DP–CP at the boundary between the edge of the metal and the semiconductor. Since the exchange of the DP–CP between the metal and semiconductor can excite free electrons in a phonon-assisted manner, the photocurrent can flow out to the external circuit if a bias voltage is applied, by which the optical energy can be converted to electrical energy. It should be noted that the energy is converted in a frequency up-converted manner because the free electrons are generated even by applying incident light whose wavelength is longer than λ_c. Figure 1.45a shows the SEM image of a metallic Au electrode whose edge has been sharpened. Figure 1.45b shows the dependences of the photocurrent on the bias voltage and the wavelength of the incident light. From these experimental results, it was confirmed that the long-wavelength cut-off was extended up to at least 532 nm.

There are at least two methods of increasing the conversion efficiency of photodetecting devices, including photovoltaic devices and solar cell batteries. For solar cell batteries, the first method is to increase the efficiency within the visible range, i.e., the wavelength range shorter than that of the absorption band edge of the material to be used as an active medium. This method has been conventionally employed; however, it is reaching fundamental and technical limits. The second method is to utilize the infrared component of the solar energy whose wavelength is longer than the absorption band edge. This method is effective to increase the conversion efficiency because sunlight contains large numbers of photons in the infrared region. Since most of the materials to be used as the active media (Si, P3HT, and so on) for solar cell batteries are active only in the visible region, they must be replaced by other exotic materials, e.g., compound semiconductors, to utilize the infrared photons. However, they are often toxic or rarely excavated. Instead, the examples (1) and (2) reviewed above demonstrated that the infrared photons can be utilized, even by using nontoxic and commonly produced conventional materials, if a nanometric structure is formed on the electrode, while the semiconductor materials remained untreated. Due to this technological advantage, nanophotonics can enable novel device functions by using conventional materials, which can realize qualitative innovations in optical technology. In the other words, nanophotonics is not a conventional material technology but a novel *size- and conformation-controlling technology* to enable novel device functions even by using conventional materials.

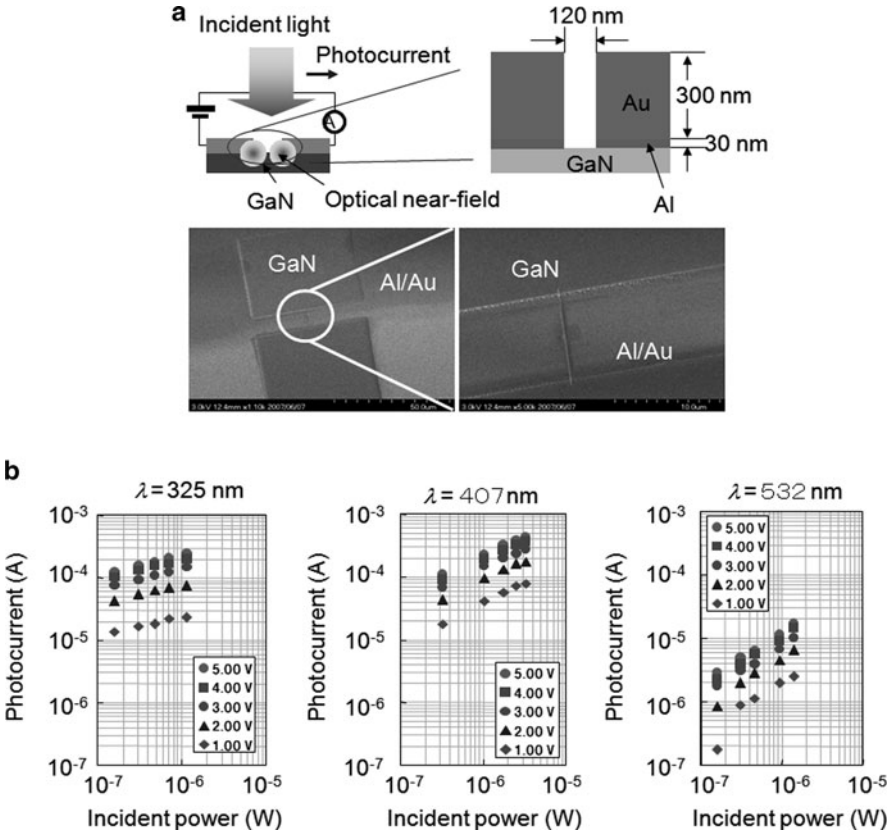

Fig. 1.45 (**a**) Cross-sectional structure of an MSM photodetector and SEM image of metallic Au electrodes 9 μm in length with a gap of 120 nm. (**b**) Relation between the incident light power and the photocurrent for incident light wavelengths of 325, 407, and 532 nm. The values of the bias voltage are also shown in the inset

1.7 Nanophotonic Systems and Their Evolution to Related Sciences

Nanophotonics has realized both quantitative and qualitative innovations. For example, novel architectures have been proposed for optical signal transmission systems, and their performance has been confirmed experimentally. They include computing using nanophotonic switches and an optical nano-fountain [68], as well as data broadcasting using multiple nanophotonic switches [69]. Quantitative innovations have been realized by decreasing the device size and power consumption beyond the diffraction-limit. More importantly, qualitative innovations have been realized by exploiting the novel functions of nanophotonic devices, which are otherwise impossible using conventional photonic devices. Quantitative innovations have already

been realized by breaking the diffraction-limit of optical/magnetic hybrid disk storage density (refer to Sect. 1.3). Qualitative innovations have also been proposed by applying the hierarchy inherent in optical near-fields to memory retrieval [70].

An example of evolution to a related science is atom photonics, in which the thermal motions of neutral atoms in a vacuum are controlled using optical near-fields [71]. Theoretical studies have examined single-atom manipulation based on the dressed photon model [72], and experimental studies have involved the first successful guidance of an atom through a hollow optical fiber [73]. Recent studies have examined atom-detecting devices [74], atom deflectors [75], and an atomic funnel [76]. Atom photonics will open up a new field of science that examines the interactions between dressed photons and single atoms.

Basic research in nanophotonics is being actively carried out. An optical near-field problem has been formulated in terms of the Carniglia–Mandel model as a complete and orthogonal set that satisfies the infinite planar boundary conditions between a dielectric and a vacuum. This approach has revealed interesting atomic phenomena occurring near the surface, which have been analyzed based on an angular spectrum representation [77, 78]. For example, optical radiation from an excited molecule on a substrate surface has been analyzed, and the results agreed quantitatively with experimental results [79]. A self-consistent, nonlocal, semiclassical theory of light–matter interactions has been developed to discuss the optical response of a variety of nanostructures [80]. In particular, the size dependence and allowance of a dipole-forbidden transition in a nanometric quantum dot system were noted [81, 82]. The optical manipulation of nanometric objects in superfluid helium has been investigated based on nonlocal semiclassical theory [83]. Electron transport through molecular bridges connecting nanoscale electrodes has been formulated [84], and a unified method has been proposed to treat extended and polaron-like localized states coupled with molecular vibrations. A one-dimensional molecular bridge made of thiophene molecules has been analyzed numerically. The study of optical near-fields associated with molecular bridges is now underway. In addition, as basic experimental work, desorption and ionization assisted by optical near-fields have been carried out, and their application to mass spectroscopy has been proposed [85, 86]. From both fundamental and applied perspectives, the role of spin degrees of freedom in excitation energy transfer driven by optical near-fields is an intriguing and important issue. A new approach has been proposed to discuss spin information achieved by energy transfer in a quantum dot pair and the effects of spin relaxation due to interactions with the environment [87, 88].

1.8 Summary

By combining the concepts of quantum field theory, optical science, and condensed-matter physics, the author has studied nanometric materials and optical energy transfer in nanometric space. Through these studies, a theoretical picture of dressed photons was obtained. Based on this picture, the exchange of dressed photons was

studied, revealing energy transfer to electric dipole-forbidden energy levels. Furthermore, the possibility of coupling a dressed photon with a coherent phonon was found, revealing a novel phonon-assisted process in light–matter interactions in nanometric space. These discoveries were applied to develop novel technologies, such as devices, fabrication techniques, energy conversion, information systems, architectures and algorithms.

Fundamental concepts such as the behavior of photons in nanometric space, excitation transfer and relaxation in a nanometric space, and the primary mechanisms of the phonon-assisted process should be delved into more deeply. Such fundamental studies are expected to bring about further discoveries involving the coupling of dressed photons with various elementary excitations besides coherent phonons, leading to the discovery of novel applications. This marriage of basic studies and technological applications is expected to establish a new field of dressed photon science and technology in the near future.

Dressed photons can be utilized to establish fundamental new technologies that can replace a wide range of conventional optical technologies. Even though users will not notice their existence, it is expected that technologies exploiting dressed photons will be widely used in everyday life in the near future. This is because dressed photons can be generated universally on the surface of illuminated nanometric materials.

The name "nanophotonics" is occasionally used for photonic crystals, plasmonics, metamaterials, silicon photonics, and quantum dot lasers using conventional propagating light. Here, one should consider the stern warning by Shannon on the casual use of the term "information theory," which was a trend in the study of information theory during the 1950s [89]. The term "nanophotonics" has been used in a similar way, although some work in "nanophotonics" is not based on optical near-field interactions. For the true development of nanophotonics, one needs deep physical insight into the behavior of virtual photons and the nanometric subsystem composed of electrons and photons.

Acknowledgements The author sincerely thanks Prof. K. Kitahara (International Christian University) and Prof. M. Tsukada (Tohoku Univ.) for their encouragement throughout his study of nanophotonics and dressed photon science and technology. He also thanks Profs. H. Hori, K. Kobayashi, I. Banno (University of Yamanashi), Profs. T. Yatsui, T. Kawazoe (University of Tokyo), Prof. M. Naruse (National Institute for Communication Technology and University of Tokyo), and Drs. W. Nomura, N. Tate, and K. Kitamura (University of Tokyo) for their collaboration.

References

1. M. Ohtsu, T. Kawazoe, T. Yatsui, M. Naruse, IEEE J. Sel. Top. Quant. Electron. **14**, 1404 (2008)
2. M. Ohtsu, K. Kobayashi, T. Kawazoe, T. Yatsui, M. Naruse, in *Preface*. Principles of Nanophotonics (Tailor & Francis, FL, 2008), pp. ix–x

3. M. Ohtsu, in *Preface to Volume V*, ed. by M. Ohtsu. Progress in Nano-Electro-Optics V (Springer, Berlin, 2006), pp. VII–VIII
4. MIT Microphotonics Center, Communication Technology Roadmap (2005), http://mph-roadmap.mit.edu/
5. K. Kobayashi, S. Sangu, H. Ito, M. Ohtsu, Phys. Rev. A **63**, 013806 (2001)
6. M. Ohtsu, K. Kobayashi, *Optical Near Fields* (Springer, Berlin, 2004), pp. 109–120
7. Y. Tanaka, K. Kobayashi, J. Microsc. **229**, 228 (2008)
8. A. Sato, Y. Tanaka, F. Minami, K. Kobayashi, J. Luminescence **129**, 1718 (2009)
9. S. Mononobe, in *Near-Field Optical Fiber Probes and the Imaging Application*, ed. by M. Ohtsu. Progress in Nano-Electro-Optics III (Springer, Berlin, 2005), pp. 1–56
10. M. Ohtsu, *Near-Field Nano/Atom Optics and Technology* (Springer, Berlin, 1998), pp. 33–69
11. E. Betzig, J.K. Trautman, Science **257**, 189 (1992)
12. U. Maheswari Rajagopalan, S. Mononobe, K. Yoshida, M. Yoshimoto, M. Ohtsu, Jpn. J. Appl. Phys. **38**, 6713 (1999)
13. K. Matsuda, T. Saiki, H. Saito, K. Nishi, Appl. Phys. Lett. **76**, 73 (2000)
14. H. Fukuda, T. Saiki, M. Ohtsu, Sensors Mater. **13**, 445 (2001)
15. N. Hosaka, T. Saiki, J. Microsc. **202**, 362 (2001)
16. T. Ushiki, Scanning near-field optical/atomic force microscopy in biology, Presented at the 5th Asia-Pacific Conference on Near-Field Optics. Optical Society of Japan, Niigata, Japan, Paper 2-1, 15–17 November 2005
17. Y. Narita, T. Tadokoro, T. Ikeda, T. Saiki, S. Mononobe, M. Ohtsu, Appl. Spectros. **52**, 1141 (1998)
18. F. Sato, Jasco Report, **46**, 34 (2004)
19. C. Hubert, G. Lerondel, R. Bachelot, S. Kostcheev, J. Grand, A. Vial, D. Barciesi, P. Royer, S.H. Chang, S.K. Gray, G.P. Wiederrecht, G.C. Shatz, Near-field photochemical imaging of noble metal nano-object using an azodyne polymer: From single to near field coupled objects, presented at the 5th Asia-Pacific Conference on Near-Field Optics. Optical Society of Japan, Niigata, Japan, Paper 3-4, 15–17 November 2005
20. T. Yatsui, M. Kourogi, M. Ohtsu, Appl. Phys. **73**, 2090 (1998)
21. T. Yatsui, M. Ohtsu, in *High-Throughput Probes for Near-Field Optics and Their Applications*, ed. by M. Ohtsu. Progress in Nano-Electro-Optics I (Springer, Berlin, 2003), pp. 1–28
22. T. Yatsui, M. Kourogi, K. Tsutsui, M. Ohtsu, J. Takahashi, Opt. Lett. **25**, 1279 (2000)
23. M. Ohtsu, Nanophotonics and application to future storage technology, Technical Digest, The Joint International Symposium on Optical Memory and Optical Data Storage 2008, (ISOM/ODS'08), HI, USA, pp. 24–26 (paper number MA01 TD0501), 13–17 July 2008
24. H. Hieda, in *Nanopatterned Media for High-Density Storage*, ed. by M. Ohtsu. Nanophotonics and Nanofabrication (Wiley-VCH, Weinheim, 2009), pp. 147–165
25. T. Nishida, T. Matsumoto, F. Akagi, H. Hieda, A. Kikitsu, K. Naito, T. Koda, N. Nishida, H. Hatano, M. Hirata, J. Nanophoton. **1**, 011597 (2007)
26. T. Nishida, T. Matsumoto, F. Akagi, in *Nanoophotonics Recording Device for High-Density Storage*, ed. by M. Ohtsu. Nanophotonics and Nanofabrication (Wiley-VCH, Weinheim, 2009), pp. 167–178
27. H. Kitahara, Y. Ueno, H. Suzuki, T. Kobayashi, H. Tanaka, Y. Kojima, M. Kobayashi, M. Katsumura, Y. Wada, T. Iida, Jpn. J. Appl. Phys. **49**, 06GE02 (2010)
28. M. Ohtsu, *Technology Roadmap for Information Storage* (Optical Industry Technology Development Association, Tokyo, 2006), pp. 35–78
29. P. Kocher, J. Jaffe, B. Jun, Introduction to differential power analysis and related attacks, http://www.cryptography.com/resources/whitepapers/DPATechInfo.pdf
30. M. Naruse, H. Hori, K. Kobayashi, M. Ohtsu, Opt. Lett. **32**, 1761 (2007)
31. M. Ohtsu, K. Kobayashi, T. Kawazoe, S. Sangu, T. Yatsui, IEEE J. Sel. Top. Quant. Electron. **8**, 839 (2002)
32. T. Kawazoe, K. Kobayashi, S. Sangu, M. Ohtsu, Appl. Phys. Lett. **82**, 2957 (2003)
33. T. Yatsui, S. Sangu, T. Kawazoe, M. Ohtsu, S.J. An, J. Yoo, G.-C. Yi, Appl. Phys. Lett. **90**, 223110 (2007)

34. T. Kawazoe, K. Kobayashi, K. Akahane, M. Naruse, N. Yamamoto, M. Ohtsu, Appl. Phys. B **84**, 243 (2006)
35. A. Shojiguti, K. Kobayashi, S. Sangu, K. Kitahara, M. Ohtsu, J. Phys. Soc. Jpn. **72**, 2984 (2003)
36. T. Kawazoe, M. Naruse, M. Ohtsu, CCLEO/QELS06, paper CFE3, Baltimore, May 2006
37. W. Nomura, T. Yatsui, T. Kawazoe, M. Ohtsu, J. Nanophoton. **1**, 011591 (2007)
38. T. Yatsui, Y. Ryu, T.Morishima, W. Nomura, T. Kawazoe, T. Yonezawa, M. Washizu, H. Fujita, M. Ohtsu, Appl. Phys. Lett. **96**, 133106 (2010)
39. T. Kawazoe, K. Kobayashi, M. Ohtsu, Appl. Phys. Lett. **86**, 103102 (2005)
40. K. Akahane, N. Yamamoto, M. Naruse, T. Kawazoe, T. Yatsui, M. Ohtsu, Extended Abstracts (The 57th Spring Meeting, 2009); The Japan Society of Applied Physics and Related Societies, paper 18a-P4-19, March 2010, Kanagawa, Japan or K. Akahane, N. Yamamoto, M. Naruse, T. Kawazoe, T. Yatsui, M. Ohtsu, Abstract, SSDM 2010
41. M. Naruse, N. Tate, O plus E **32**, 145 (2010)
42. L.B. Kish, IEE Proc. Circ. Dev. Syst. **151**, 190 (2004)
43. V.P. Carey, A.J. Shah, J. Electron. Packag. **128**, 346 (2006)
44. R.H. Brown, R.Q. Twiss, Nature **178**, 1447 (1956)
45. T. Kawazoe et al., J. Nanophoton. **2**, 029502 (2008)
46. H. Hori, in *Optical and Electronic Process of Nano-Matters*, ed. by M. Ohtsu (Kluwer, Dordrecht, 2001), pp. 1–55
47. M. Naruse, T. Miyazaki, F. Kubota, T. Kawazoe, K. Kobayashi, S. Sangu, M. Ohtsu, Opt. Lett. **30**, 201 (2005)
48. T. Kawazoe, K. Kobayashi, S. Takubo, M. Ohtsu, J. Chem. Phys. **122**, 024715 (2005)
49. K. Kobayashi, A. Sato, T. Yatsui, T. Kawazoe, M. Ohtsu, Appl. Phys. Express **2**, 075504 (2009)
50. T. Kawazoe, K. Kobayashi, M. Ohtsu, Appl. Phys. B **84**, 247 (2006)
51. T. Yatsui, W. Nomura, M. Ohtsu, Nano Lett. **5**, 2548 (2005)
52. H. Yonemitsu, T. Kawazoe, K. Kobayashi, M. Ohtsu, J. Photoluminescence **122**, 230 (2007)
53. Y. Ito, S. Nakasato, R. Kuroda, M. Ohtsu, Microelectronic Eng. **84**, 705 (2007)
54. M. Koike, S. MIyauchi, K. Sano, T. Imazono, in *X-ray Devices and the Possibility of Applying Nanophotonics*, ed. by M. Ohtsu. Nanophotonics and Nanofabrication (Wiley-VCH, Weinheim, 2009), pp. 179–191
55. T. Kawazoe, H. Fujiwara, K. Kobayashi, M. Ohtsu, Appl. Phys. B **98**, 5 (2010)
56. T. Yatsui, K. Hirata, W. Nomura, Y. Tabata, M. Ohtsu, Appl. Phys. B **93**, 55 (2008)
57. M. Naruse, T. Yatsui, W. Nomura, K. Hirata, Y. Tabata, M. Ohtsu, J. Appl. Phys. **105**, 63156 (2009)
58. W. Nomura, T. Yatsui, Y. Yanase, K. Suzuki, M. Fujita, A. Kamata, M. Naruse, M. Ohtsu, Appl. Phys. B **99** 75 (2010)
59. D. Graham-Rowe, Nat. Photon. **2**, 515 (2008)
60. T. Yatsui, S. Yamazaki, K. Ito, H. Kawamura, M. Mizumura, T. Kawazoe, M. Ohtsu, Appl. Phys. B **97**, 375 (2009)
61. S. Yamazaki, T. Yatsui, M. Ohtsu, Appl. Phys. Express **1**, 061102 (2008)
62. T. Kawazoe, H. Fujiwara, K. Kobayashi, M. Ohtsu, IEEE J. Sel. Top. Quant. Electron. **15**, 1380 (2009)
63. H. Fujiwara, T. Kawazoe, M. Ohtsu, Appl. Phys. B **98**, 283 (2010)
64. H. Fujiwara, T. Kawazoe, M. Ohtsu, Appl. Phys. B **100**, 85 (2010)
65. S. Yukutake, T. Kawazoe, T. Yatsui, W. Nomura, K. Kitamura, M. Ohtsu, Appl. Phys. B **99** 415(2010)
66. S. Guenes, H. Neugebauer, S. Sariciftci, Chem. Rev. **107**, 1324 (2007)
67. S. Yamazaki, W. Nomura, T. Kawazoe, M. Ohtsu, Extended Abstracts (The 68th Autumun Meeting, 2007); The Japan Society of Applied Physics, paper number 7p-Q-10, Sapporo, Japan, September 2007
68. M. Naruse, T. Miyazaki, T. Kawazoe, K. Kobayashi, S. Sangu, F. Kubota, M. Ohtsu, IEICE Trans. Electron. **E88-C**, 18171823 (2005)
69. M. Naruse, T. Kawazoe, S. Sangu, K. Kobayashi, M. Ohtsu, Opt. Express **14**, 306 (2006)
70. M. Naruse, T. Yatsui, W. Nomura, N. Hirose, M. Ohtsu, Opt. Express **13**, 9265 (2005)

71. M. Ohtsu (ed.), *Near-Field Nano/Atom Optics and Technology* (Spinger, Berlin, 1998), pp. 218–293
72. K. Kobayashi, S. Sangu, H. Ito, M. Ohtsu, Phys. Rev. A **63**, 013806 (2001)
73. H. Ito, T. Nakata, K. Sakaki, M. Ohtsu, K. I. Lee, W. Jhe, Phys. Rev. Lett. **76**, 4500 (1996)
74. K. Totsuka, H. Ito, T. Kawamura, M. Ohtsu, J. Appl. Phys. **41**, 1566 (2002)
75. K. Totsuka, H. Ito, K. Suzuki, K. Yamamoto, M. Ohtsu, T. Yatsui, Appl. Phys. Lett. **82**, 1616 (2003)
76. A. Takamizawa, H. Ito, S. Yamada, M. Ohtsu, Appl. Phys. Lett. **85**, 1790 (2004)
77. T. Inoue, H. Hori, Phys. Rev. A **63**, 063805 (2001)
78. T. Inoue, H. Hori, in *Quantum Theory of Radiation in Optical Near Field Based on Quantization of Evanescent Electromagnetic Waves Using Detector Mode*, ed. by M. Ohtsu. Progress in Nano- Electro-Optics IV (Springer, Berlin 2005), pp. 127–199
79. T. Inoue, H. Hori, IEICE Trans. Electron. **E88-C**, 1836 (2005)
80. K. Cho, Progr. Theor. Phys. Suppl. **106**, 225 (1991)
81. H. Ishihara, K. Cho, Phys. Rev. B **48**, 7960 (1993)
82. K. Cho, Y. Ohfuti, K. Arima, Surf. Sci. **363**, 378 (1996)
83. T. Iida, H. Ishihara, IEICE Trans. Electron. **E88-C**, 1809 (2005)
84. K. Mitsutake, M. Tsukada, e-J. Surf. Sci. Nanotechnol. **4**, 311 (2006)
85. L.C. Chen, J. Yonehama, T. Ueda, H. Hori, K. Hiraoka, J. Mass Spectrom. **42**, 346 (2007)
86. L.C. Chen, T. Ueda, M. Sagisaka, H. Hori, K. Hiraoka, J. Phys. Chem. **111**, 2409 (2007)
87. A. Sato, F. Minami, K. Kobayashi, Physica E, **40**, 313 (2007)
88. A. Sato, F. Minami, H. Hori, K. Kobayashi, J. Comput. Theor. Nanoscience **7**, 1–10 (2010)
89. C.E. Shannon, IEEE Trans. Inform. Theor. **IT-2**, 3 (1956)

http://www.springer.com/978-3-642-17480-3

Progress in Nanophotonics 1
Ohtsu, M. (Ed.)
2011, XIV, 238 p., Hardcover
ISBN: 978-3-642-17480-3